POPULATION BOUNDARIES AND GRAVITATIONAL-WAVE TEMPLATES FOR EVOLVING WHITE DWARF BINARIES.

A Dissertation

Submitted to the Graduate Faculty of the
Louisiana State University and
Agricultural and Mechanical College
in partial fulfillment of the
requirements for the degree of
Doctor of Philosophy

in

The Department of Physics and Astronomy

by
Ravi Kumar Kopparapu
B.Sc., Nagarjuna University, 1996
M.Sc., University of Pune, 1998
M.S., Louisiana State University, 2003
December, 2006

Dedication

To my parents, Mallika & Sarma, for their endless love and support...

Acknowledgements

First of all, I would like to thank Prof. Joel E. Tohline for his wonderful guidance and most importantly for his unlimited patience. He is what I think is an accomplished teacher and a role model. This research started with a very simple task of generating a sine-wave, as a first step into the field of gravitational-wave astronomy. Later, it extended to the field of theoretical astrophysics and took the shape of what is presented in this dissertation.

I would also like to thank Prof. Frank for his very insightful thoughts and encouragement in group meetings and in personal discussions. I very much appreciate the support and guidance of Prof. Gabriela González for providing me the opportunity to take part in the gravitational-wave data analysis group. I am indebted to Patrick Motl, a post-doc in our group, for his early morning 'chats' which helped me with a different perspective of thinking. I am grateful to Shangli Ou, another post-doc in our group, for his adivce and friendship in the time of need. Many of my fellow students, along with me, had great fun at LSU. The names here are by no means comprehensive : Vayujeet Gokhale, Mario D'Souza, Karly Pitman, Xiaomeng Peng, Wesley Even, Charles Bradley, Chad Hanna, Andy Rodriguez and Ilsoon Park. Finally, I owe a great deal of gratitude to my wife, Varada, for taking care of me and my daughter all these years.

This work has been supported, in part, by funds from the U.S. National Science Foundation grants AST-0407070 and PHY-0326311, and in part by funds from NASA through grant NAG5-13430.

Table of Contents

List of Tables

List of Figures

Abstract

We present results from our analysis of double white dwarf (DWD) binary star systems in the inspiraling and mass-transfer stages of their evolution. Theoretical constraints on the properties of the white dwarf stars allow us to map out the DWD trajectories in the gravitational-wave amplitude-frequency domain and to identify population boundaries that define distinct sub-domains where inspiraling and/or mass-transferring systems will and will not be found. We identify for what subset of these populations it should be possible to measure frequency changes and, hence, directly follow orbit evolutions given the anticipated operational time of the proposed space-based gravitational-wave detector, LISA. We show how such measurements should permit the determination of binary system parameters, such as luminosity distances and chirp masses, for mass-transferring as well as inspiraling systems.

We also present results from our efforts to generate gravitational-wave templates for a subset of mass-transferring DWD systems that fall into one of the above mentioned sub-domains. Realizing that the templates from a point-mass approximation prove to be inadequate when the radii of the stars are comparable to the binary separation, we build an evolutionary model that includes finite-size effects such as the spin of the stars and tidal and rotational distortions. In two cases, we compare our model evolution with three-dimensional hydrodynamical models of mass-transferring binaries to demonstrate the accuracy of our results. We conclude that the match is good, except during the final phase of the evolution when the mass transfer rate is rapidly increasing and the mass donating star is severely distorted.

1. Part I : Introduction

White dwarf stars are thought to be the end products of the evolution of a normal star, such as our sun (Fowler, 1926; Bessell, 1978). The first white dwarf star, Sirius B, was discovered in 1844 by an astronomer, Friedrich Bessel, and is a companion to the brightest star in the sky (Sirius A), which is at a distance of about 8 light years from Earth. He noticed that the light observed from Sirius A has an oscillatory motion, as though it is being pulled back and forth by an unseen object. In 1862, Alvan Clark resolved this object for the first time and found that this unseen object (Sirius B) has a surface temperature of 25,000 Kelvin (the sun's surface temperature $\approx$ 5,800 Kelvin) and is nearly 10,000 times fainter than Sirius A. To put it in another way, though Sirius B is a very hot star, it appears to be fainter even at the same distance as Sirius A. This means that Sirius B has to have a much smaller radius than Sirius A. In addition, from observing the orbital motion of this binary system, it was later found that Sirius B has a mass roughly the same as our sun packed into a volume that is roughly the same as the Earth. The implication of these observations is that Sirius B is an unusually compact object with an average density of about million times greater than our sun. Since the discovery of Sirius B, astronomers have found many white dwarfs (Liebert, 1980) and discovered that they are common in our Galaxy.

1.1 Formation of White Dwarf Stars

Astronomers frequently represent the properties and evolution of stars in a plot that is called the Hertzsprung-Russel (H-R) diagram, first proposed in 1910 by Ejnar Hertzsprung and Henry Norris Russel. Theoretically, it is a plot of luminosity (energy radiated per second) of a star versus its effective temperature[1]. In general ordinary stars, such as our

[1]According to Shu (1982), effective temperature is defined as the surface temperature of a star if it were a blackbody radiating at its given luminosity.

sun, begin their life by igniting nuclear fusion of hydrogen into helium in their cores. This stage of burning hydrogen is the longest period all stars spend in their entire life time and on the H-R diagram they fall along a diagonal band called the "main-sequence (MS)." On the main-sequence the distinguishing factor for stars is their individual masses. Some stars are more massive than others and the more massive ones also are more luminous. It was Eddington who first noticed that the luminosity of a star is proportional to its mass to the fourth power ($L \propto M^4$). This means that a star 10 times more massive than the sun radiates 10^4 times more energy every second. Because it expends this energy faster, the more massive star evolves faster than a low mass star.

Let us consider a normal, low mass star such as our sun. Once it starts fusing hydrogen to helium inside the core, it settles onto the main-sequence and stays there for most of its life. After exhausting hydrogen in its core, there is no more nuclear energy generation in the core and the core contracts gravitationally. At the same time, the envelope of the star expands and its temperature decreases. The star moves to the right of the H-R diagram to what is referred to as the "sub-giant" branch. This decrease in the temperature of the star causes it to appear *red* and after some time the expansion of the star pushes it onto the "red-giant" branch of the H-R diagram. At the same time the helium core continues to contract and the electrons in the core are so tightly packed that they become degenerate. This degeneracy results due to Pauli's exclusion principle, which states that no two electrons can have the same quantum state (so that they are placed in consecutive energy levels, starting from the ground state). The pressure produced can be understood from the Heisenberg uncertainty relation, which states that the position and momentum of a particle cannot be simultaneously determined. This means that a gas of free electrons exhibits degeneracy pressure (due to large momentum arising from uncertainty principle) independent of the temperature.

For stars in the red-giant phase, eventually the outer envelope expands and leaves the star, forming a planetary nebula. The hot (inert) helium core that is unveiled is called a

"white dwarf". For stars more massive than the sun, the process of core contraction will further lead to fusion of helium into carbon and oxygen (CO) and a CO core is formed. This type of compact star is referred to as a carbon-oxygen white dwarf star. White dwarfs are located in the low luminosity, high temperature region of the H-R diagram.

1.2 Properties of White Dwarf Stars

For MS stars, the radius is proportional to their mass. So, for example, a $0.1M_{\odot}$ star has roughly $1/10^{th}$ the radius of our sun. But white dwarfs have a curious relationship that the mass of a white dwarf is inversely proportional to its radius. So a more massive white dwarf star has a smaller radius, and vice versa. But there is a limit on how massive a white dwarf can be. In 1931 Chandrasekhar (Chandrasekhar, 1931) showed that the radius of a white dwarf decreases to zero at a mass of $1.2M_{\odot}$ (called the Chandrasekhar mass $M_{\rm ch}$; the modern adopted value is $M_{\rm ch} = 1.44M_{\odot}$). In 1983 he was awarded the Noble prize in physics in part for this discovery. This is the maximum mass a white dwarf can have under degenerate conditions. To this day, all the observed white dwarfs have been found to have masses at or below this limit.

1.3 Formation of Double White Dwarf Stars

Normal MS stars can form as binary (or higher multiple) systems during their birth and each star in such system will evolve off the main-sequence during the course of its evolution. If both the stars in the system are low mass stars, it is reasonable to expect over time the system will naturally evolve into a double white dwarf (DWD) pair. The possible formation mechanism is as follows (Evans et al., 1987): In a binary system with MS stars, the more massive component first evolves off the MS as the hydrogen in its core is exhausted due to conversion into helium. At the same time, by expanding its envelope, the star starts to

fill its Roche lobe[2] and transfers mass to its companion (the yet unevolved main-sequence star). This companion then fills *its* Roche surface with the new material it acquired and a common envelope is formed. Due to drag forces (as the stars are orbiting each other in a common envelope), the heat generated is utilized in shedding the envelope. But this energy has to come from the binding energy of the orbit, so the binary shrinks. At this point, the system has a degenerate helium core and a main-sequence star in a closer orbit than before. Eventually, the remaining main-sequence star also evolves as it uses up hydrogen in the core and expands. But it expands to a smaller radius to fill its Roche lobe than the previous one, as the stars are closer to each other (the Roche lobe is now smaller for this second star). A second common envelope phase ensues, shrinking the orbit even further and drives off the envelope. What remains now is a system with two degenerate (helium) cores in a tighter orbit. The same scenario can be applied to understand the formation of short period carbon-oxygen (CO) or carbon-helium (CO + He) binary white dwarfs if the initial MS stars are more massive.

1.4 Evolution of Double White Dwarf Stars

Once a binary star system reaches the stage where two degenerate cores are orbiting one other, it appears that no other (stellar) evolutionary mechanism will influence the orbit of the binary and it may live forever in a detached state. But, of course, the universe is not boring and a completely different type of evolution enters the scene. In fact, this "new" type of evolution existed all the while in the background, but we had to wait until the final stages of stellar evolution to notice the effects.

In 1905, Einstein proposed the general theory of relativity[3] which stated that (1) gravity

[2]A Roche lobe is an equipotential surface around a star within which the material is bound to that star. A more detailed description is given in Chapter 2. Also, see Frank et al. (2001) for more information.

[3]A graduate course introduction to relativity I found useful is the online course by Sean Carroll. http://pancake.uchicago.edu/ carroll/notes/

is a manifestation of space-time (four dimensional world = three space co-ordinates + one time co-ordinate) curvature and (2) there is a relation between matter and the curvature of space-time. Newtonian gravity is a subset of this theory in the limit of weak curvature. If the curvature is disturbed or oscillates due to motion of the matter, the resulting ripples are the gravitational waves.

Gravitational waves travel with the speed of light and they carry away angular momentum from any system that experiences sufficiently asymmetric matter oscillations. Binary stars are examples of such systems. The orbital angular momentum $J_{\rm orb}$ for a binary system in circular orbit may be written as

$$J_{\rm orb} = M_1 M_2 \Big(\frac{G\ a}{M_{\rm tot}} \Big)^{1/2}, \tag{1.1}$$

where M_1 and M_2 are the masses of the components in the binary, $M_{\rm tot} = M_1 + M_2$ is the total mass in the system, a is the separation between the components and G is the universal gravitational constant. If there is no change in the masses of the individual components, then $M_{\rm tot}$ is constant. So, as $J_{\rm orb}$ decreases the separation also decreases. Hence, for the detached DWD binary discussed above, gravitational radiation provides a means to evolve the system further.

In the case of binary neutron stars (or pulsars, which are even more compact than white dwarfs), of course, gravitational radiation also serves as a driving mechanism for binary evolution to smaller and smaller orbits. The most famous example is the Hulse-Taylor pulsar (Hulse & Taylor, 1975), discovered by Russell Hulse and Joseph Taylor in 1975. After many years of observations they proved that the binary orbit is decaying through a loss of angular momentum in accordance with the rate predicted by general relativity. For this discovery they were awarded the Nobel prize in physics in 1993.

In the quadrupole approximation to the General theory of relativity (Peters & Mathews, 1963; Thorne, 1987; Finn & Chernoff, 1993), the time-dependent gravitational-wave strain

(amplitude), $h(t)$, generated by a point-mass binary system in circular orbit has two polarization states. The plus (+)and cross (×) polarizations of $h(t)$ generically take the respective forms,[4,5]

$$h_+ = h_{\rm norm}\cos[\phi(t)] \qquad \text{and} \qquad h_\times = h_{\rm norm}\sin[\phi(t)]\,, \tag{1.2}$$

where the time-dependent phase angle,

$$\phi(t) = \phi_0 + 2\pi\int f(t)dt\,, \tag{1.3}$$

where ϕ_0 is the phase at time $t = 0$, $f = \Omega_{\rm orb}/\pi$ is the frequency of the gravitational wave measured in Hz, $\Omega_{\rm orb}$ is the angular velocity of the binary orbit given in radians per second, and the characteristic amplitude of the wave,

$$\begin{aligned} h_{\rm norm} &= \frac{G}{rc^4}\,\frac{4\Omega_{\rm orb}^2 M_1 M_2 a^2}{(M_1+M_2)} \\ &= \frac{4}{rc^4}\Big(\frac{G^5}{M_{\rm tot}}\Big)^{1/3} M_1 M_2 \pi^{2/3} f^{2/3} \end{aligned} \tag{1.4}$$

where c is the speed of light and r is the distance to the source. If the principal parameters of the binary system (such as frequency and masses) do not change with time, then f and $h_{\rm norm}$ will both be constants and the phase angle ϕ will vary only linearly in time, so the source will emit "continuous-wave" radiation. In this case, the gravitational-wave signal from the binary system is just a sin or cos function, as given in Eq.(1.2) and illustrated in Fig.1.1. If, however, any of the binary parameters — M_1, M_2, a, or $\Omega_{\rm orb}$ — vary with time, then $h_{\rm norm}$ and/or f will also vary with time in accordance with the physical process that causes the variation.

[4]Appendix A provides more details on the derivation of these expressions.

[5]Throughout our discussion when we refer to experimental measurements of h, we will assume that the binary system is being viewed "face on" so that the measured peak-to-peak amplitudes of the two polarization states are equal and at their maximum value, given by $h_{\rm norm}$. If the orbit is inclined to our line of sight, the inclination angle can be determined as long as a measurement is obtained of both polarization states as shown, for example, by Finn & Chernoff (1993). Because our discussion focuses on Galactic DWD binaries, we will also assume that the effects of cosmological expansion on measured signal strengths is negligible.

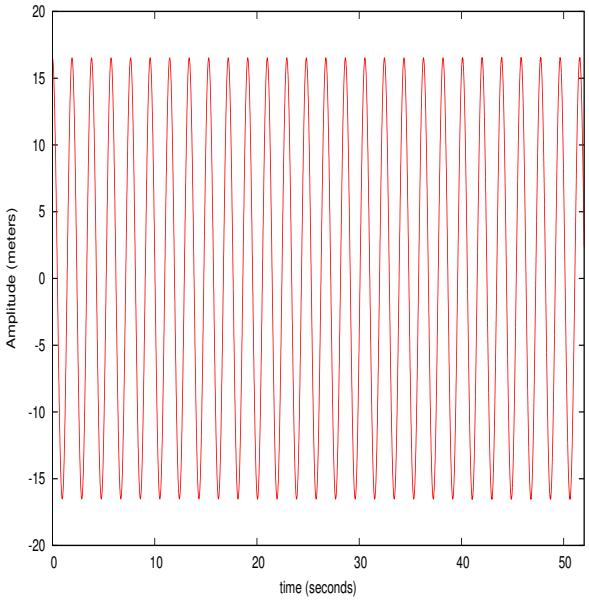

Figure 1.1: Gravitational-wave signal from a non-inspiralling system.

In a detached binary system, the orbital angular momentum is carried away by gravitational waves and so the stars inspiral toward each other as a function of time. This loss in angular momentum causes the separation between the stars to slowly decrease (increasing frequency) with time. Since the individual masses are not changing, we can deduce from Eq.(1.4) that $h_{\rm norm} \propto f^{2/3}$. Hence an inspiralling binary system produces an ever increasing amplitude and frequency of gravitational waves. This characteristic feature of increasing frequency and amplitude is called a "chirp signal" as illustrated here in Fig.1.2. In the case of binary neutron stars, this chirping is most prominent in the high frequency range (10 Hz - 10 kHz) of the gravitational-wave spectrum and eventually the two stars collide and merge. DWD binaries also undergo the chirping phase (the orbit keeps shrinking) but the corresponding gravitational-wave radiation is most prominent in the lower frequency (10^{-4} Hz - 1 Hz) end of the spectrum. Once the two stars are close enough to one another, the lower mass white dwarf star (the donor) fills its Roche lobe[6] (this is because it has the larger radius) and starts transferring mass to its companion (accretor). This system is now called

[6]A more detailed description of Roche lobe is given in §2.1.

a "semi-detached" system. If both the stars are filling their Roche lobes, then it is called a "contact binary". At the Roche lobe contact stage for DWD systems, the mass ratio deter-

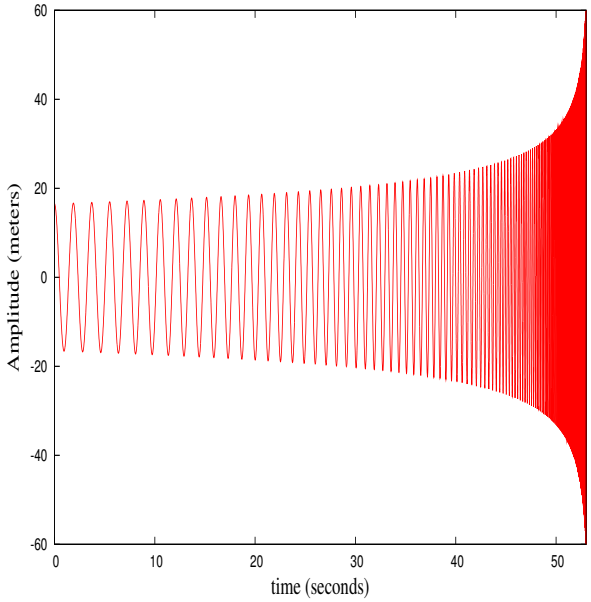

Figure 1.2: Gravitational-wave signal from an inspiralling system.

mines the fate of the binary. If the mass ratio is greater than a critical value, $q_{\rm crit}$, then the mass transfer becomes unstable[7] and the system will likely merge. If the mass ratio is less than $q_{\rm crit}$, the system may survive and reverse its evolution to longer periods (increasing separation) with stable mass transfer. It should be noted that we already have a handle on the size of the galactic population of DWD binaries from optical, UV, and x-ray observations. In the immediate solar neighborhood, there are 18 systems[8] (Nelemans, 2005; Anderson, 2005; Roelofs, 2005) known to be undergoing a phase of stable mass transfer (AM CVn being the prototype) and the ESO SN Ia Progenitor SurveY (SPY) has detected nearly 100 detached DWD systems (Napiwotzki et al., 2004b). At present, orbital periods and the component

[7]Unstable means that the mass loss rate from the donor to the accretor keeps increasing steadily.

[8]Three models (Cropper et al., 1998; Wu et al., 2002; Marsh & Steeghs, 2002) have been proposed to determine the nature of two controversial candidate systems (RX J0806+15 and V407 Vul) out of these 18, which can change the number of known AM CVn systems between 16 and 18.

masses for 24 detached DWD systems have been determined (see Table 3 of Nelemans et al. (2005) and references therein), five of which come from the SPY survey.

1.5 Significance of Detecting Gravitational Waves

- The most important contribution of gravitational waves comes from the fact that they can be used to find the sources which are not possible to detect through electromagnetic detection methods. For instance, sources like binary neutron stars or binary black holes are very hard to detect *directly* through conventional detection methods. Also electromagnetic observations are hampered by dust absorption between the source and the detector, whereas gravitational waves can pass through dust without any absorption. This will significantly increase the number of sources that can be detected compared with electromagnetic observations.

Various instruments are either already operational, such as the ground-based gravitational-wave observatory LIGO[9] (Abbott et al., 2005) operating in the high-frequency range or planned, such as the space-based observatory, LISA[10] (Faller & Bender, 1984; Evans et al., 1987; Bender, 1998) operating in the low frequency band. In this dissertation we are concentrating on DWD systems, which are prominent in the low frequency band of the gravitational-wave spectrum and, hence, they are one of the most promising sources for LISA. If, as has been predicted (Iben & Tutukov, 1984, 1986), close DWD pairs are the end product of the thermonuclear evolution of a sizeable fraction of all binary systems, then DWD binaries must be quite common in our Galaxy and the gravitational waves (GW) emitted from these systems may be a dominant source of background noise for LISA in its lower frequency band, $f \lesssim 3 \times 10^{-3}$ Hz (Hils et al., 1990; Cornish & Larson, 2003). DWD binaries are also believed to be (one of the likely) progenitors of Type Ia supernovae (Iben

[9] http://www.ligo.caltech.edu
[10] http://lisa.nasa.gov

& Tutukov, 1984; Branch et al. , 1995; Tout, 2005) in situations where the accreting white dwarf exceeds the Chandrasekhar mass limit, collapses toward nuclear densities, then explodes. Because its instruments will have sufficient sensitivity to detect GW radiation from close DWD binaries throughout the volume of our Galaxy, LISA will provide us with an unprecedented opportunity to study this important tracer of stellar populations and it will provide us with a much better understanding of the formation and evolution of close binary systems in general. Clearly, a considerable amount of astrophysical insight will be gained from studying the DWD population as a guaranteed source for LISA.

1.6 Parameterization

In this section we define a variety of physical parameters that will be used throughout upcoming chapters. Here we will only be considering the evolution of DWD systems in which the basic system parameters vary on a timescale that is long compared to $1/f$.

As mentioned in the previous sections, the less massive star in a DWD binary will always have the larger radius. Therefore, in a DWD system that is undergoing mass transfer, we can be certain that the less massive star is the component that is filling its Roche lobe and is transferring (donating) mass to its companion (the more massive, accretor). With this in mind, throughout the remainder of our discussion we will identify the two stars by the subscripts d (for donor) and a (for accretor), rather than by the less descript subscripts 1 and 2, and will always recognize that the subscript d identifies the less massive star in the DWD system. This notation will be used even during evolutionary phases (such as a gravitational-wave-driven inspiral phase) when the two stars are detached and therefore no mass-transfer is taking place. Furthermore, we will frequently refer to the mass ratio of the system,

$$q \equiv \frac{M_d}{M_a}\,, \tag{1.5}$$

Table 1.1: $rh_{\rm norm}$ and f in terms of system parameters.

Specify:	$J_{\rm orb}$	a	$\Omega_{\rm orb}$
(1)	(2)	(3)	(4)
$rh_{\rm norm}$	$\frac{4}{c^4}G^3M_{\rm tot}^5J_{\rm orb}^{-2}Q^3$	$\frac{4}{c^4}G^2M_{\rm tot}^2a^{-1}Q$	$\frac{4}{c^4}(GM_{\rm tot})^{5/3}\Omega_{\rm orb}^{2/3}Q$
f	$\frac{1}{\pi}G^2M_{\rm tot}^5J_{\rm orb}^{-3}Q^3$	$\frac{1}{\pi}(GM_{\rm tot})^{1/2}a^{-3/2}$	$\frac{1}{\pi}\Omega_{\rm orb}$

which will necessarily be confined to the range $0 < q \leq 1$ because $M_d \leq M_a$. Also, it will be understood that the limiting mass for either white dwarf is $M_{\rm ch}$. For the first part of this dissertation, we will assume that Kepler's 3$^{\rm rd}$ Law provides a fundamental relationship between the angular velocity and the separation of DWD binaries, that is,

$$\Omega_{\rm orb}^2 = \frac{GM_{\rm tot}}{a^3}\,. \tag{1.6}$$

Relation (1.6) allows us to replace either $\Omega_{\rm orb}$ or a in favor of the other parameter in Eq. (1.4). Furthermore, we will find it useful to interchange one or both of these parameters with the binary system's orbital angular momentum as defined by Eq.(1.1) which, via the above relations, can be expressed in any of the following forms:

$$J_{\rm orb} = M_{\rm tot}a^2\Omega_{\rm orb}Q = (GM_{\rm tot}^3a)^{1/2}Q = \left(\frac{G^2M_{\rm tot}^5}{\Omega_{\rm orb}}\right)^{1/3}Q\,, \tag{1.7}$$

where,

$$Q \equiv \frac{q}{(1+q)^2}\,, \tag{1.8}$$

is the ratio of the system's reduced mass to its total mass.

Table 1.1 summarizes how the frequency f and dimensional amplitude $rh_{\rm norm}$ of the gravitational-wave strain can be expressed in terms of $M_{\rm tot}$, Q, and either $J_{\rm orb}$, a, or $\Omega_{\rm orb}$. We note as well that the so-called "chirp mass" $\mathcal{M}$ of a given system (Finn & Chernoff, 1993) is obtained from $M_{\rm tot}$ and Q via the relation,

$$\mathcal{M} = M_{\rm tot}Q^{3/5}\,. \tag{1.9}$$

2. Evolution of DWD Binaries in the Amplitude-Frequency Domain*

As described earlier, detached DWD binaries slowly inspiral toward one another as they lose orbital angular momentum due to gravitational radiation. It is reasonable to assume that $M_{\rm tot}$ and the system mass ratio q remain constant during this phase of their evolution. Therefore, as the expressions given in column 2 of Table 1.1 show, both the frequency and amplitude of the emitted gravitational-wave signal will increase as the system's orbital angular momentum decreases. Combining these expressions in a way that cancels out the dependence on $J_{\rm orb}$, we obtain,

$$rh_{\rm norm} \;=\; \left[\frac{2^5\pi^2}{c^2}\left(\frac{GM_{\rm ch}}{c^2}\right)^5 K^5 f^2\right]^{1/3} = 5.38\ [K^5 f^2]^{1/3}\ \text{meters}\,, \tag{2.1}$$

where the dimensionless mass parameter,

$$K \equiv 2^{1/5}\left(\frac{\mathcal{M}}{M_{\rm ch}}\right) = 2^{1/5}\left(\frac{M_{\rm tot}}{M_{\rm ch}}\right)Q^{3/5} = \left(\frac{M_{\rm a}}{M_{\rm ch}}\right)\left(\frac{2q^3}{1+q}\right)^{1/5}, \tag{2.2}$$

has been defined such that it acquires a maximum value of unity in the limiting case where $M_d = M_a = M_{\rm ch}$; otherwise, $0 < K < 1$. (We note that in the limiting case of $K = 1$, the chirp mass of the system is $\mathcal{M} = 0.871 M_{\rm ch} = 1.25 M_\odot$.) From expression (2.1), we see that the trajectory of an inspiraling, detached DWD binary in the amplitude-frequency diagram can be determined without specifying precisely the rate at which angular momentum is lost from the system. Specifically, because $d\ln(rh_{\rm norm})/d\ln f = 2/3$, trajectories of inspiraling DWD binaries will be straight lines with slope 2/3 in a plot of $\log(rh_{\rm norm})$ versus $\log f$. Example evolutionary trajectories (lines with arrows pointing to the upper-right) for detached, DWD binary systems that are undergoing a GR-driven inspiral are displayed in the $\log(rh_{\rm norm}) - \log f$ diagram of Fig.(2.1), where $rh_{\rm norm}$ is specified in meters and f is specified in Hz. The

*Reproduced by permission of the AAS

three trajectories represent systems having dimensionless mass parameters $K = 0.813$ (green dashed line), 0.474 (blue dotted line), and 0.271 (pink dot-dashed line); assuming a mass ratio $q = 2/3$ for all three systems, this corresponds to total system masses of $2.4, 1.4$, and $0.8 M_{\odot}$, respectively.

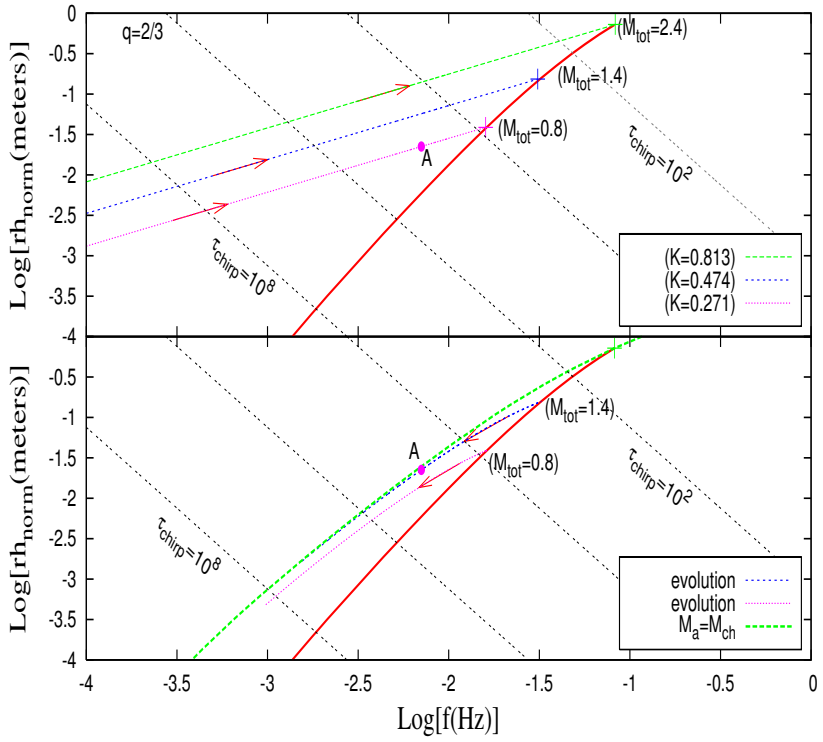

Figure 2.1: DWD evolutionary trajectories

2.1 Roche-Lobe Contact

Edouard Roche in 19^{th} century discovered that for binary star systems in circular orbits, in the reference frame that has the same angular frequency as the orbital angular frequency (so that the stars are at rest, assuming there spins are synchronized) we can define "equipotential surfaces" surrounding the stars provided the potential generated by the two stars is

equivalent to the potential of two point masses plus a centrifugal term arising due to shift into co-rotating frame. Near the stars these equipotential surfaces are spheres enclosing the respective stars at the center of the sphere. As we gradually move away from the stars, these equipotential surfaces intersect first at a point called the " Lagrange point (L1 point)" and if we slice these surfaces along the equatorial plane they look like a figure eight shape, as shown in Fig.(2.2). The volume enclosed by these equipotential surfaces at the first contact is called a "Roche lobe". Material inside the Roche lobe of a star is bound equally to that respective star but material *on* the surface of the Roche lobe is bound to both the stars. If the star overflows its Roche lobe, then it starts transferring mass to the companion through the L1 point.

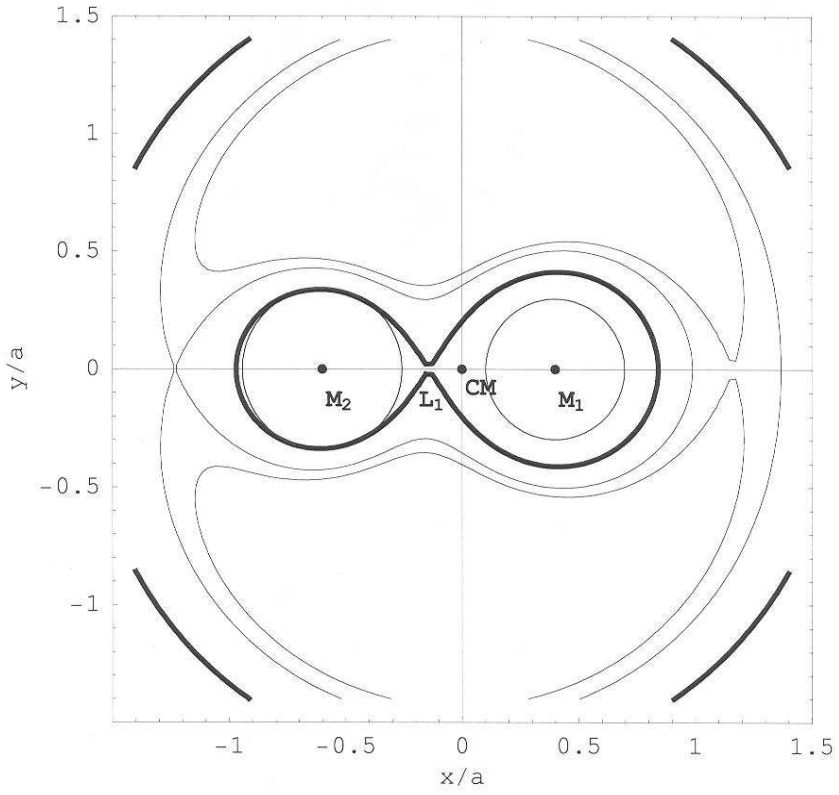

Figure 2.2: Equipotential surfaces and Roche lobe

The detached inspiral phase of the evolution of a DWD binary will terminate when the binary separation a first becomes small enough that the less massive white dwarf fills its Roche lobe. From the mass-radius relationship for zero-temperature white dwarfs (Nauenberg, 1972; Marsh et al., 2004) we know that the radius of the donor R_d is,

$$\frac{R_d}{R_\odot} = 0.0114\Big[\Big(\frac{M_d}{M_{\rm ch}}\Big)^{-2/3} - \Big(\frac{M_d}{M_{\rm ch}}\Big)^{2/3}\Big]^{1/2}\Big[1 + 3.5\Big(\frac{M_d}{M_{\rm p}}\Big)^{-2/3} + \Big(\frac{M_d}{M_{\rm p}}\Big)^{-1}\Big]^{-2/3}, \qquad (2.3)$$

where $M_p \equiv 0.00057\ M_\odot$. Furthermore, from Eggleton (1983) we find that the Roche-lobe radius R_L is,

$$R_{\rm L} \approx a\Big[\frac{0.49\ q^{2/3}}{0.6\ q^{2/3} + \ln(1+q^{1/3})}\Big] = \frac{J_{\rm orb}^2}{GM_{\rm tot}^3}\frac{(1+q)^4}{q^2}\Big[\frac{0.49\ q^{2/3}}{0.6\ q^{2/3} + \ln(1+q^{1/3})}\Big]. \qquad (2.4)$$

The orbital separation – and the corresponding gravitational-wave amplitude $rh_{\rm norm}$ and frequency f – at which the inspiral phase terminates can therefore be determined uniquely for a given donor mass M_d and system mass ratio q by setting $R_d = R_L$ and combining expressions (2.3) and (2.4) accordingly. The termination points of the three inspiral trajectories — marked by plus symbols in the top panel of Figure 2.1 — have been calculated in this manner. The solid red curve connecting the sequence of plus symbols in Figure 2.1 traces out the locus of points that define the termination points of the detached inspiral phase of numerous other DWD systems that have mass ratios $q = 2/3$ but that have values of $M_{\rm tot}$ ranging from 2.4 $M_\odot$ to 0.06 $M_\odot$.

2.2 Evolution to Lower Frequencies Due to Conservative Mass Transfer (CMT)

After the less massive, donor star fills its Roche lobe and starts transferring mass to its companion, the evolution of the DWD system in the amplitude-frequency domain will deviate significantly from the inspiral trajectory. If the system initial mass ratio is less than some critical value $q_{\rm crit}$, it is generally thought that the ensuing mass-transfer phase will be stable

(Marsh et al., 2004; Gokhale et al., 2007) and that the system will evolve in such a way that the donor stays in marginal contact with its Roche lobe. As the system evolves, the mass ratio q will steadily decrease, the binary separation a will steadily increase, and the gravitational-wave amplitude and frequency will both steadily decrease. Without knowing the precise rate at which this phase of stable mass transfer proceeds, we can map out the evolutionary trajectory of various sytems in the $\log(rh_{\rm norm})-\log f$ diagram by again combining expressions (2.3) and (2.4) via the constraint $R_d = R_{\rm L}$ and by demanding that, as q decreases, the system mass $M_{\rm tot}$ remains constant ("conservative mass trasnfer), that is, $M_d = qM_{\rm tot}/(1+q)$. By way of illustration, the bottom panel of Figure 2.1 shows two such stable, conservative mass-transfer (CMT) trajectories that have been calculated in this manner: The blue dotted trajectory is for a system of mass $M_{\rm tot} = 1.4\ M_\odot$; the pink dotted trajectory is for a system of mass $M_{\rm tot} = 0.8\ M_\odot$. As the arrows indicate, along both mass-transfer trajectories evolution is down and to the left in this amplitude-frequency diagram. We have assumed that both of these systems began the mass-transfer phase of their evolution with an initial mass ratio $q_0 = 2/3$. Hence, the starting point of both trajectories lies on the termination boundary for inspiralling systems having mass ratios of $q = 2/3$.

If the DWD system mass $M_{\rm tot} < M_{\rm ch}$ (as is the case for both of the evolutionary trajectories plotted in the bottom panel of Figure 2.1), the CMT phase of the system's evolution can in principle proceed uneventfully to a very low value of q, that is, the donor's mass can practically shrink to zero. However, if $M_{\rm tot} > M_{\rm ch}$, the mass of the accretor will exceed the Chandrasekhar mass limit when q drops below the value,

$$q_{\rm ch} \equiv \frac{M_{\rm tot}}{M_{\rm ch}} - 1\,, \qquad \text{for } M_{\rm tot} > M_{\rm ch}\,. \tag{2.5}$$

With the expectation that something catastrophic (*e.g.*, a Type Ia supernova explosion) will occur when the accretor's mass exceeds the Chandrasekhar mass limit, it is reasonable to assume that mass-transfer trajectories with $M_{\rm tot} > M_{\rm ch}$ will terminate at a point in

the amplitude-frequency diagram that is marked by this critical value of the system mass ratio. The locus of points that is defined by the termination points of these trajectories defines another interesting astrophysical boundary in the amplitude-frequency diagram. This termination boundary has been drawn as a thick, (green) dashed curve in the bottom panel of Figure 2.1.

2.3 Boundaries in the Amplitude-Frequency Domain

The inspiral trajectory drawn for $K = 0.813$ ($M_{\rm tot} = 2.4\ M_{\odot}$) and the curve marking the termination of various inspiral trajectories in the top panel of Figure 2.1 define boundaries in the amplitude-frequency domain outside of which no DWD system should exist if it has a mass ratio $q \leq 2/3$. As explained above, DWD evolutionary trajectories are expected to "bounce" off of the high-frequency "termination" boundary and thereafter move toward lower frequencies because, at that boundary, mass transfer begins. And to exist above the $K = 0.813$ inspiral trajectory, the more massive star would have to have a mass $M_a > M_{\rm ch}$ if $q = 2/3$. Analogous domain boundaries can be constructed readily for other values of the system mass ratio q. (See Figure 4.1 for examples.) For each value of q, the shapes of the bounding curves are roughly the same as shown in the top panel of Figure 2.1, but for higher values of q the right-hand termination boundary shifts to higher frequencies and the limiting inspiral trajectory (set by a higher value of the mass parameter K) shifts to higher strain amplitudes; for lower values of q the termination boundary shifts to lower frequencies and the limiting inspiral trajectory shifts to lower strain amplitudes. Given our present understanding of the structure of white dwarfs, it seems extremely unlikely that any DWD binary systems can exist outside of the domain that is defined by the bounding curves for systems with $q = 1$ (see, for example, the outermost boundaries drawn in Figure 4.1 for systems at a distance of 10 kpc).

2.4 Non-uniqueness of Points in the Amplitude -Frequency Diagram

Specifying the amplitude $rh_{\rm norm}$ and frequency f of the gravitional-wave radiation that is being emitted from a DWD system does not, in itself, provide sufficient information to permit a unique determination of the individual masses of the stars in the system. This is illustrated by the point marked "A" in Figure 2.1. In both panels of the figure, point "A" sits at the same position in the amplitude-frequency diagram ($rh_{\rm norm} = 2.25 \times 10^{-2}$ meters; $f = 7.068 \times 10^{-3}$ Hz), but in the top panel it represents one point along the inspiral trajectory of a detached DWD system that has $M_{\rm tot} = 0.8 M_\odot$ and $q = 2/3$ ($M_a = 0.48 M_\odot$, $M_d = 0.32 M_\odot$), whereas in the bottom panel it represents one point along the evolutionary trajectory of a mass-transferring, semi-detached DWD system that has $M_{\rm tot} = 1.4 M_\odot$ and $q = 0.118$ ($M_a = 1.252 M_\odot$, $M_d = 0.148 M_\odot$). At best, a given point in the amplitude-frequency diagram provides a determination of the dimensionless mass parameter K, as defined by Eq. (2.2); at point "A," for example, $K = 0.271$. But a DWD system that, from observations, has been determined to sit at point "A" could have any of a wide variety of combinations of $M_{\rm tot}$ and q that satisfy Eq. (2.2) with this value of K. Knowing the value of K alone does not even permit us to differentiate between a system that is in the inspiral phase of its evolution or one that is undergoing a phase of mass transfer. As we illustrate in §4.2, if LISA data analysis efforts are able to detect evolutionary changes in individual DWD system — measure, for example, the time-rate-of-change of the gravitational-wave frequency — it may be possible to lift this degeneracy. We note, in particular, that the sign of the frequency variation may delineate the underlying physical processes that are driving the system's evolution.

3. Time-Dependence*

Up to this point, we have described key features of DWD evolutionary trajectories in the amplitude-frequency diagram without referring to the rate at which the evolution of any given system proceeds. Here we investigate the time scales on which significant changes in various system parameters and, as a consequence, the rate at which measurable changes in the gravitational-wave signature occur. Drawing on the expressions given in column 2 of Table 1.1, we can write the time-rate of change of the amplitude and frequency of the gravitational-wave strain as follows:

$$\frac{d\ln h_{\rm norm}}{dt} = 5\frac{\partial \ln M_{\rm tot}}{\partial t} - 2\frac{\partial \ln J_{\rm orb}}{\partial t} + 3\frac{\partial \ln Q}{\partial t}\,; \tag{3.1}$$

$$\frac{d\ln f}{dt} = 5\frac{\partial \ln M_{\rm tot}}{\partial t} - 3\frac{\partial \ln J_{\rm orb}}{\partial t} + 3\frac{\partial \ln Q}{\partial t}\,. \tag{3.2}$$

Adopting the assumption that the binary system's total mass is conserved during either the GR-driven inspiral phase or a phase of stable CMT, we can drop the first term on the right-hand-side of both of these equations to obtain,

$$\frac{d\ln h_{\rm norm}}{dt} \approx -2\frac{\partial \ln J_{\rm orb}}{\partial t} + 3\frac{\partial \ln Q}{\partial t}\,; \qquad \frac{d\ln f}{dt} \approx -3\frac{\partial \ln J_{\rm orb}}{\partial t} + 3\frac{\partial \ln Q}{\partial t}\,. \tag{3.3}$$

These expressions can be used to deduce the rate of change of $h_{\rm norm}$ and f during a phase of stable mass transfer when the system mass ratio (and, hence, the mass-ratio function Q) is steadily changing and, simultaneously, the system is losing angular momentum due to the radiation of gravitational waves. On the other hand, during a phase of GR-driven inspiral, both stars in the DWD binary are detached from their respective Roche lobes so, although orbital angular momentum is being steadily lost from the system, q (hence, Q) is not changing and the following, even simpler expressions apply:

$$\frac{d\ln h_{\rm norm}}{dt} \approx -2\frac{\partial \ln J_{\rm orb}}{\partial t}\,; \qquad \frac{d\ln f}{dt} \approx -3\frac{\partial \ln J_{\rm orb}}{\partial t}\,. \tag{3.4}$$

*Reproduced by permission of the AAS

3.1 GR-Driven Inspiral

During the inspiral phase of the evolution of DWD binaries, the evolution is driven entirely by the loss of angular momentum due to gravitational radiation. According to Peters & Mathews (1963) (see also Misner et al. (1973)), starting at time $t = 0$ from any orbital separation a_0 – and corresponding orbital angular momentum J_0, strain amplitude h_0, and strain frequency f_0 – to a high degree of precision the time-dependent behavior of $J_{\rm orb}$ is described by the relation,

$$J_{\rm orb}(t) = J_0(1 - t/\tau_{\rm chirp})^{1/8}\,, \tag{3.5}$$

where the inspiral evolutionary time scale is,

$$\tau_{\rm chirp} \;\equiv\; \frac{5}{256}\frac{c^5 a_0^4}{G^3 M_{\rm tot}^3}\Big[\frac{(1+q)^2}{q}\Big] = \frac{5}{64\pi^2}\Big(\frac{c}{r h_0 f_0^2}\Big)\,. \tag{3.6}$$

Conveniently, according to the last expression in Eq. (3.6), the evolutionary time scale $\tau_{\rm chirp}$ for a given DWD system is completely specified once the position of the system in the $\log(r h_{\rm norm}) - \log f$ diagram is known. In fact, in this amplitude-frequency diagram, curves of constant $\tau_{\rm chirp}$ are straight lines of slope minus two. For reference, several different "chirp isochrones" have been drawn as dotted lines of slope -2 in both panels of Figure 2.1; they identify systems for which $\tau_{\rm chirp} = 10^8, 10^6, 10^4$ and 10^2 years. We note in particular that for the point labeled "A" in Figure 2.1, $\tau_{\rm chirp} = 6.7 \times 10^4$ years.

Clearly, for the typical properties that are associated with DWD binaries, only very small changes will occur in the orbital parameters of any given system during a single year of observation. Hence, a reasonably accurate expression for $J_{\rm orb}(t)$ can be obtained by expanding Eq. (3.5) in powers of $t/\tau_{\rm chirp}$ and keeping only the leading order, time-dependent term, that is,

$$J_{\rm orb}(t) \approx J_0\Big[1 - \frac{1}{8}\Big(\frac{t}{\tau_{\rm chirp}}\Big)\Big]\,, \tag{3.7}$$

or,

$$\frac{\partial \ln J_{\rm orb}}{\partial t} \approx -\frac{1}{8\tau_{\rm chirp}}\,. \tag{3.8}$$

Therefore, from Eq. (3.4) we deduce,

$$\frac{d\ln h_{\rm norm}}{dt} \approx +\frac{1}{4\tau_{\rm chirp}} \qquad \text{(inspiral phase)}\,; \tag{3.9}$$

$$\frac{d\ln f}{dt} \approx +\frac{3}{8\tau_{\rm chirp}} \qquad \text{(inspiral phase)}\,. \tag{3.10}$$

By way of illustration, based on this result the arrow pointing up and to the right in Figure 3.1 illustrates how far a system initially located at the point marked "A" in Figure 2.1 will move in the amplitude-frequency diagram in 10,000 years if it is evolving through point "A" along an inspiral trajectory.

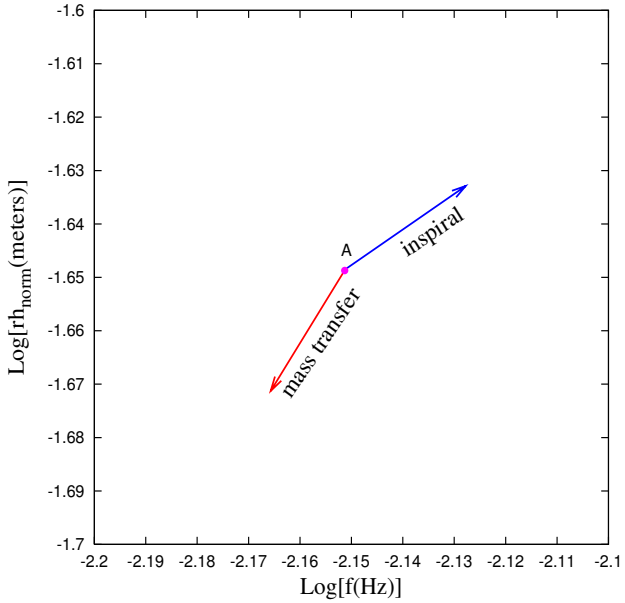

Figure 3.1: Magnified view of point A

3.2 Conservative Mass Transfer

If a DWD system with initial mass ratio q_0 is undergoing mass transfer at a constant rate,

$$\mu \equiv -\dot{M}_d\,, \tag{3.11}$$

where $\dot{M}_d \equiv dM_d/dt$ is understood to be intrinsically negative, but otherwise the system conserves its total mass (*i.e.*, $\dot{M}_a = -\dot{M}_d = \mu$), then the system mass ratio will vary with time according to the relation,

$$q(t) \;=\; \frac{q_0 - t/\tau_{\rm mt}}{1 + t/\tau_{\rm mt}}, \tag{3.12}$$

where,

$$\tau_{\rm mt} \equiv \frac{M_{\rm tot}}{\mu}\Big(\frac{1}{1+q_0}\Big)\,. \tag{3.13}$$

Hence, from Eq. (1.8), the time-dependent behavior of the ratio of the system's reduced mass to its total mass,

$$Q(t) = Q_0\Big[1 - \Big(\frac{1-q_0}{q_0}\Big)\frac{t}{\tau_{\rm mt}} - \frac{1}{q_0}\Big(\frac{t}{\tau_{\rm mt}}\Big)^2\Big]\,. \tag{3.14}$$

From the work of Webbink & Iben (1987) and Marsh et al. (2004), we deduce that the timescale governing the evolution of semi-detached DWD binaries that are undergoing a phase of stable mass transfer is,

$$\tau_{\rm mt} \approx \Big(\frac{4\Delta\zeta}{q_0}\Big)\tau_{\rm chirp}\,, \tag{3.15}$$

where $\Delta\zeta$ is a parameter that is of order unity for the majority of systems that are of interest to us here (see Appendix B for the definition of $\Delta\zeta$ and a derivation of Eq. 3.15. It should be emphasized that a phase of stable CMT can occur only if $\Delta\zeta$ is positive and, hence, only if $q < q_{\rm crit}$. Representative values of $q_{\rm crit}$ are given in Table B.1 of Appendix B). It is significant, although not surprising, that the timescale on which DWD systems evolve during a phase of stable CMT is roughly the same as the timescale on which they evolve during the inspiral phase. Ultimately, both evolutionary phases are driven by the loss of angular momentum due to gravitational radiation. It is for this reason that we have drawn various "chirp isochrones" in the bottom panel as well as the top panel of Figure 2.1.

Combining Eq. (3.15) with Eq. (3.14), we find that,

$$Q(t) \approx Q_0\Big[1 - \Big(\frac{1-q_0}{4\Delta\zeta}\Big)\frac{t}{\tau_{\rm chirp}} - \frac{q_0}{16(\Delta\zeta)^2}\Big(\frac{t}{\tau_{\rm chirp}}\Big)^2\Big]\,, \tag{3.16}$$

which implies,

$$\frac{\partial \ln Q}{\partial t} \approx -\Big(\frac{1-q_0}{4\Delta\zeta}\Big)\frac{1}{\tau_{\rm chirp}}\,. \tag{3.17}$$

Inserting this expression along with expression (3.8) into Eq. (3.3) we therefore deduce that,

$$\frac{d\ln h_{\rm norm}}{dt} \approx \frac{1}{4\tau_{\rm chirp}}\Big[1-3\frac{(1-q_0)}{\Delta\zeta}\Big] \qquad \text{(mass-transfer phase);} \tag{3.18}$$

$$\frac{d\ln f}{dt} \approx \frac{3}{8\tau_{\rm chirp}}\Big[1-2\frac{(1-q_0)}{\Delta\zeta}\Big] \qquad \text{(mass-transfer phase).} \tag{3.19}$$

We see from Figure B.1 in Appendix B that all DWD binary systems have values of $\Delta\zeta < (\Delta\zeta)_B \equiv 2(1-q)$. Hence, the second term inside the square brackets on the right-hand-side of both Eq. (3.18) and Eq. (3.19) is larger in magnitude than unity, so $d\ln f/dt$ and $d\ln h_{\rm norm}/dt$ are both negative. This supports in a quantitative way our earlier qualitative conclusion that, in contrast to the inspiral phase, during a phase of stable mass transfer the frequency and amplitude of the gravitational-wave signal will decrease with time. In an effort to illustrate this point explicitly, the arrow pointing down and to the left in Figure 3.1 shows how far a system with $M_{\rm tot} = 1.4M_\odot$ that is initially located at point "A" will move in the amplitude-frequency diagram in 10,000 years if it is evolving through point "A" along a stable CMT trajectory.

4. Detectability of DWD Systems*

Whether or not a given DWD system will be detectable by LISA will depend on the level of noise in the detector as well as on the strength and the stability of the DWD system's gravitational-wave signal. In order to aid in our discussion of the detectability of such systems, therefore, we have combined in Figure 4.1 the theoretically derived domain boundaries displayed in Figure 2.1 with a LISA noise curve. This noise curve is generated using an online sensitivity curve generator[9] with the standard LISA observatory parameters (assuming a one year of signal integration and the signal-to-noise ratio (SNR) is set to one). In transferring the theoretical curves to Figure 4.1, in which the vertical scale is h instead of (rh), we have adopted a distance to all sources of 10 kpc. Also, in addition to displaying the domain boundaries for DWD systems that have a mass ratio $q = 2/3$ (long dashed curves), Figure 4.1 contains analogous domain boundaries calculated for systems with $q = 1$ (short dashed curves) and $q = 1/5$ (dotted curves). For reference purposes, the point marked "A" in Figure 2.1 has been transferred to Figure 4.1 as well.

In order to estimate the SNR that a given source will exhibit in the LISA data after one full year of signal integration, it is tempting to simply measure the distance $\Delta \log h$ between the amplitude $h_{\rm source}$ of the source in the strain-frequency diagram and the level $h_{\rm noise}$ of the LISA noise curve at the same frequency. For example, a DWD system represented by point "A" in Figure 4.1 would be estimated to have a $\mathrm{SNR_{YR}} = h_{\rm source}/h_{\rm noise} = 10^{\Delta \log h} \approx 10^{1.6} \approx 40$. Using this method of estimating the signal-to-noise ratio, the top curve in the bottom panel of Figure 4.2 shows what $\mathrm{SNR_{YR}}$ would be for DWD systems that fall along the locus of inspiral termination points (curved line) for $q = 2/3$ displayed in Figure 4.1. At the high-frequency end of this inspiral termination boundary, the estimated $\mathrm{SNR_{YR}}$ climbs

*Reproduced by permission of the AAS

[9]http://www.srl.caltech.edu/%7Eshane/sensitivity/

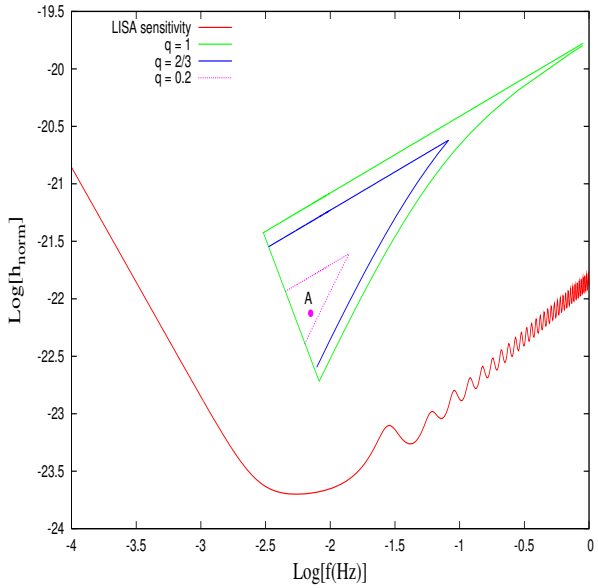

Figure 4.1: DWD boundaries in LISA's noise spectrum

well above 100, which would seem to bode well for detection by LISA. However, this estimate will be valid only if these sources emit a signal that exhibits a high degree of phase coherence throughout one full year of observation. If a loss of phase coherence limits the integration time to less than one year, then this curve provides an overly optimistic estimate of the system's SNR.

For the remainder of our discussion, we will assume that a sufficient degree of phase coherence is maintained if the observed phase $\phi_{\rm O}$ minus the theoretically computed phase $\phi_{\rm C}$ does not differ by more than $\pi/2$ radians.[10] For various DWD systems and assumed gravitational-wave templates we will calculate the amount of time $t_{\rm O-C}$ required for the "O-C" phase difference to reach $\pi/2$ and, if $t_{\rm O-C} < 1$ yr, we will scale the LISA one-year noise curve to the shorter time before estimating the SNR of that system. Specifically, relative to the signal-to-noise ratio derived from the one-year LISA noise curve, $\rm SNR_{YR}$, the signal-to-

[10]This assumes that LISA will be able to determine to an accuracy ΔN of one quarter of one orbit precisely how many orbits N an individual DWD system completes over the time period of LISA's observations; in one year, for example, DWD systems with $f \sim 10^{-3} - 10^{-2}$Hz, will complete $\sim 10^4 - 10^5$ orbits. This value of the phase shift is somewhat arbitrary, but based on other discussions (e.g., Stroeer et al. (2005)) it represents a conservative estimate of LISA's capabilities.

noise ratio expected for an integration time of $t_{\mathrm{O-C}}$ will be provided by the expression (Seto, 2002),

$$\mathrm{SNR} = \mathrm{SNR}_{\mathrm{YR}}\left(\frac{t_{\mathrm{O-C}}}{1\ \mathrm{yr}}\right)^{1/2}. \tag{4.1}$$

4.1 Systems With Non-negligible Frequency Variations

As we have discussed, the physical processes that drive the evolution of DWD binaries operate on a "chirp" timescale, and τ_{chirp} is typically much longer than one year. Hence, the time-variation of a given system's gravitational-wave frequency $f(t)$ can be well approximated by a truncated Taylor series expansion in time and, using Eq. (1.3), the observed phase of the gravitational-wave signal ϕ_{O} can be written in the form (Stroeer et al., 2005),

$$\phi_{\mathrm{O}}(t) = \phi_0 + 2\pi f_0 t + 2\pi \sum_{k=1}^{k_{\mathrm{max}}} \frac{t^{k+1}}{(k+1)!} f^{(k)}\,, \tag{4.2}$$

where f_0 is the signal frequency at time $t = 0$, and the "spin-down parameters" $f^{(k)} \equiv d^k f/dt^k (k = 1, \ldots, k_{\mathrm{max}})$. If, for example, the Taylor series can be truncated at $k_{\mathrm{max}} = 1$ and this observed signal is compared to a computed template that assumes a continuous-wave signal and therefore has a phase that increases only linearly with time, $\phi_{\mathrm{C}}(t) = (\phi_0 + 2\pi f_0 t)$, the amount of time for the O-C phase difference to reach $\pi/2$ will be,

$$t_{\mathrm{O-C}} = \left(2\ |f^{(1)}|\right)^{-1/2}. \tag{4.3}$$

From Eqs. (3.10) and (3.19) we see that, for both the inspiral and CMT phases of DWD evolutions, the first time-derivative of the frequency can be written in the form,

$$f^{(1)} \approx \frac{3 f_0}{8\tau_{\mathrm{chirp}}}\Big[1 - 2g\Big], \tag{4.4}$$

where, respectively,

$$g = 0 \qquad \text{(inspiral phase)}; \tag{4.5}$$

$$g = \frac{(1-q_0)}{\Delta\zeta} \qquad \text{(mass-transfer phase)}. \tag{4.6}$$

Hence, we can write,

$$t_{\mathrm{O-C}} = \left(\frac{4\tau_{\mathrm{chirp}}}{3|1-2g|f_0}\right)^{1/2} = \left[\frac{5}{48\pi^2|1-2g|}\left(\frac{c}{rh_0f_0^3}\right)\right]^{1/2}. \tag{4.7}$$

As an illustration, in the top panel of Figure 4.2 we have plotted the function $t_{\mathrm{O-C}}(f)$ for DWD binaries that lie along the segment joining inspiral termination points ($q = 2/3$) shown in Figure 4.1. Over this entire range of frequencies, $t_{\mathrm{O-C}} \leq 1$ year; indeed, at the highest frequencies $t_{\mathrm{O-C}}$ drops well below one week. Combining this calculation of $t_{\mathrm{O-C}}$ with expression (4.1) produces the lower (red) curve in the bottom panel of Figure 4.2. This curve provides a more realistic estimate of the SNR that DWD systems of this type (that lie at a distance of 10 kpc) will exhibit in LISA data if they are assumed to be continuous-wave sources. In the frequency range of 10^{-1} - 10^{-2} Hz, they will have roughly an order of magnitude lower SNR than one would estimate from a simple measurement of $\Delta \log h$ in Figure 4.1. For these systems, the higher SNR depicted by the upper (green) curve in the bottom panel of Figure 4.2 will be realized only if a proper inspiral template is used during data analysis to ensure that phase coherence of the signal is maintained over a full year of signal integration.

If the function g in Eq. (4.7) is independent of h and f — as is the case for the inspiral phase of DWD evolutions — then curves of constant $t_{\mathrm{O-C}}$ in the amplitude-frequency diagram will be straight lines having a slope of -3. In Figure 4.1 we have drawn a line segment of slope -3 that identifies which inspiral systems have $t_{\mathrm{O-C}} = 1$ year. Inspiral systems that lie below and to the left of this line segment have $t_{\mathrm{O-C}} > 1$ year, while systems that lie above and to the right have $t_{\mathrm{O-C}} < 1$ year. Hence, any inspiral system that lies inside of the triangular regions identified in Figure 4.1 will lose phase coherence in less than one year of observation if one assumes that they emit continuous-wave radiation. An analogous one-year demarcation boundary can be drawn for DWD binaries that are undergoing a phase of stable CMT by evaluating Eq. (4.7) using the function $g(q, M_{\mathrm{tot}})$ given by expression (4.6).

Because this function generally is of order unity, however, the one-year demarcation boundary for mass-transferring systems is generally well-approximated by the line segment that marks the one-year demarcation boundary for inspiral systems. We conclude, therefore, that if LISA is to achieve its optimal source detection performance throughout the triangular-shaped regions of the strain-frequency domain shown in Figure 4.1, the LISA data will need to be analyzed with a proper bank of frequency-varying strain templates.

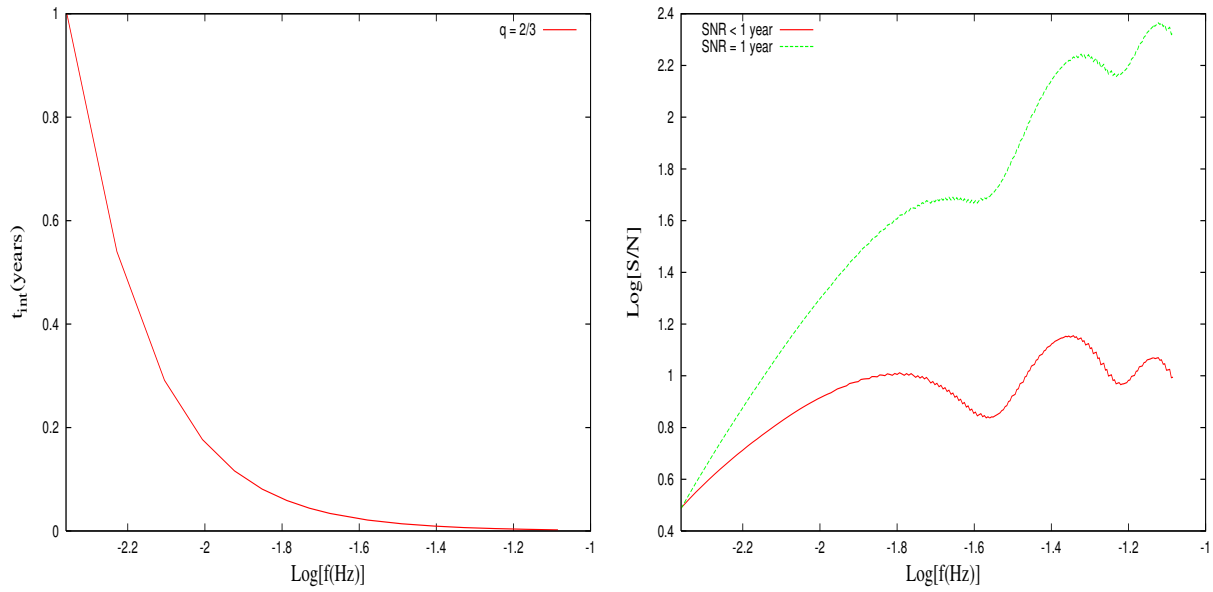

Figure 4.2: Integration times & signal to noise ratio.

4.2 Determination of Distance and Chirp Mass

An analysis of a one-year-long LISA data stream that utilizes a proper set of frequency-varying strain templates should be able to determine the rate at which the strain frequency and, hence, the orbital frequency is changing in DWD binaries that are identified as sources in the triangular regions of the parameter space shown in Figure 4.1. When used in conjunction with the measurement of h_0 and f_0, an accurate measurement of $f^{(1)}$ for any source will

permit a determination of the distance to the source r and the binary system's chirp mass $\mathcal{M}$ or the individual component masses of the binary system, as follows.

Equation (2.1) provides a relation between the three unknown binary system parameters $r, M_{\rm tot}$ and q, and the experimentally measurable parameters f and $h_{\rm norm}$, namely,

$$\frac{M_{\rm tot}^5}{r^3}\Big[\frac{q}{(1+q)^2}\Big]^3 \;=\; \frac{\mathcal{M}^5}{r^3} = \frac{c^{12}}{2^6\pi^2 G^5}\Big[\frac{h_{\rm norm}^3}{f^2}\Big]\,. \tag{4.8}$$

A second relation between the unknown astrophysical parameters and measurable ones is provided by combining the derived expression for $f^{(1)}$ in Eq. (4.4) with the definition of $\tau_{\rm chirp}$ given in Eq. (3.6). Specifically, we obtain,

$$r(1-2g) = \frac{5c}{24\pi^2}\Big[\frac{f^{(1)}}{h_{\rm norm} f^3}\Big]\,, \tag{4.9}$$

where, in general, g is a nontrivial function of $M_{\rm tot}$ and q. With only two equations, of course, it is not possible to uniquely determine all three of the binary's primary system parameters. During the inspiral phase of a DWD evolution, however, $g = 0$, so a fortunate situation arises. Equation (4.9) drops its explicit dependence on the system mass to give a clean determination of r. But once r has been determined, Eq. (4.8) gives only the chirp mass $\mathcal{M}$, rather than giving $M_{\rm tot}$ and q separately. This is a familiar result (Schutz, 1986).

During the CMT phase of an evolution, the function $g(M_{\rm tot}, q)$ is nonzero so Eq. (4.9) does not provide an explicit determination of r. However, the requirement that $R_d = R_L$ provides an important additional physical relationship between the unknown astrophysical parameters and measurable ones. Specifically, by setting R_d from Eq. (2.3) equal to R_L from Eq. (2.4) and using Kepler's law to write a in terms of f, we obtain,

$$\Big[\frac{R_\odot^3}{GM_\odot}\Big]^{1/2} f \;=\; \Big[\pi^2 (0.0114)^3 \frac{M_{\rm ch}}{M_\odot}\Big]^{-1/2} \frac{M_{\rm tot}}{M_\odot}\Big(\frac{q}{1+q}\Big) H(M_d, q)\,, \tag{4.10}$$

where,

$$\begin{aligned} H(M_d, q) \;\equiv\; & \Big(\frac{1+q}{q}\Big)^{1/2}\Big[\frac{0.49\; q^{2/3}}{0.6\; q^{2/3} + \ln(1+q^{1/3})}\Big]^{3/2}\Big[1 - \Big(\frac{M_d}{M_{\rm ch}}\Big)^{4/3}\Big]^{-3/4} \\ & \times\Big[1 + 3.5\Big(\frac{M_d}{M_{\rm p}}\Big)^{-2/3} + \Big(\frac{M_d}{M_{\rm p}}\Big)^{-1}\Big]\,. \end{aligned} \tag{4.11}$$

Hence, taken together, Eqs. (4.8)-(4.10) can be used to determine all three primary system parameters – r, $M_{\rm tot}$, and q – from the three measured quantities, $h_{\rm norm}$, f, and $f^{(1)}$. (We stress that this method of determining the values of the primary system parameters is only valid in situations where $q < q_{\rm crit}(M_{\rm tot})$, as explained in Appendix A.)

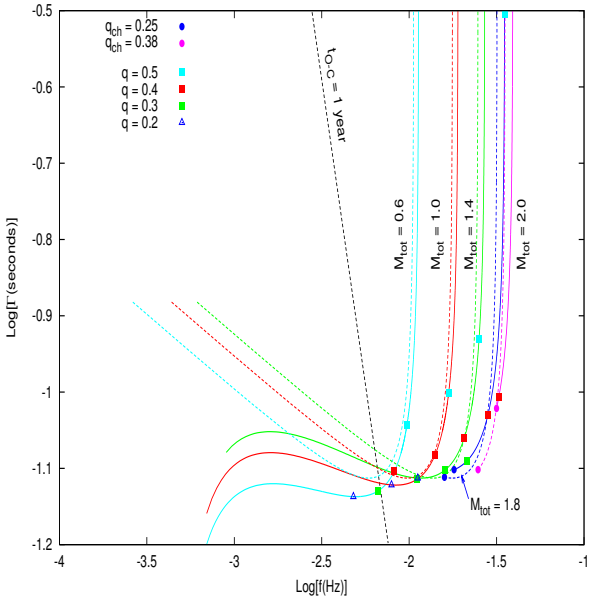

Figure 4.3: Determination of mass parameters from f and $\dot{f}$

We are unable to solve this set of equations analytically due to the complexity of the functions $g(M_{\rm tot}, q)$ and $H(M_d, q)$. However, the formulae that Paczyński (1967) adopted for $R_d(M_d)$ and $R_L(q)$ (see Appendix E) lead to much simpler expressions for both of these functions, namely, $g = [\frac{3}{2}(1-q)/(2-3q)]$ and $H = 1$. As is shown in Appendix E, in this case Eqs. (4.8)-(4.10) can be combined to give Eq. (E.17), which provides the following analytic expression for the mass ratio q in terms of f and $f^{(1)}$:

$$q^2(1+q)\left(1-\frac{3}{2}q\right)^3 = \left[\frac{2^{12}3^3\pi^8\alpha^5}{5^3c^{15}}\right]\frac{f^{16}}{[-f^{(1)}]^3}\,, \tag{4.12}$$

where $\alpha \equiv 0.0141(GM_\odot R_\odot^3)^{1/2}$. Once q is known, r can be obtained using Eq. (4.9) in conjunction with Paczyński's $g(q)$ relation; then $M_{\rm tot}$ can be obtained from Eq. (4.8). Specifi-

cally, from relations (E.14) and (E.16) we obtain, respectively,

$$r = \frac{5c}{24\pi^2}\left[\frac{-f^{(1)}}{h_{\rm norm} f^3}\right](2-3q)\,; \tag{4.13}$$

$$M_{\rm tot} = \left[\frac{5^3 c^{15}}{2^{15}\cdot 3^3 \pi^8 G^5}\right]^{1/5}\left\{\frac{(1+q)^6(2-3q)^3}{q^3}\cdot\frac{[-f^{(1)}]^3}{f^{11}}\right\}^{1/5}. \tag{4.14}$$

For any $M_{\rm tot} \leq 2M_{\rm ch}$, these three equations are valid for mass ratios over the range $0 < q < 2/3$ because, for Paczyński's model, $q_{\rm crit} = 2/3$ independent of $M_{\rm tot}$ (see Appendix A).

The solid curves in Figure 4.3 illustrate results obtained numerically from a self-consistent solution of Eqs. (4.8)-(4.10); the dashed curves illustrate results obtained analytically from expressions (4.12) and (4.14). Across the parameter domain defined by the two observables $\log(f)$ and $\log(\Gamma)$ — where

$$\Gamma \equiv \{[-f^{(1)}]^3/f^{16}\}^{1/10} \tag{4.15}$$

is measured in seconds — each curve traces a constant $M_{\rm tot}$ "trajectory" with the system mass ratio q varying along each curve, as indicated. At high frequencies, each curve begins at a value of q that is slightly below $q_{\rm crit}$; at low frequencies, the curves have been extended down to $q = 0.05$, unless $M_{\rm tot} > M_{\rm ch}$, in which case the curve has been terminated at the value $q = q_{\rm ch}$, as given by Eq. (2.5). The general behavior of these curves can best be understood by analyzing analytic expression (4.12). Over the relevant range of mass ratios $0 \leq q \leq q_{\rm crit} = 2/3$, the analytic function,

$$\Gamma_{\rm anal} = 0.0521\left[q^2(1+q)\left(1-\frac{3}{2}q\right)^3\right]^{-1/10} \ \text{seconds}\,, \tag{4.16}$$

reaches a minimum value ($\Gamma_{\rm min} = 0.077$ seconds) when $q = q_{\rm extreme}$, where

$$q_{\rm extreme} \equiv \frac{1}{12}(\sqrt{41}-3) = 0.2836\,. \tag{4.17}$$

Moving from high frequency to low frequency along each $M_{\rm tot}$ "trajectory," the function Γ steadily drops until $q = q_{\rm extreme}$ and $\Gamma = \Gamma_{\rm min}$. (This behavior holds for the solid curves

as well as the dashed curves, although the precise values of $\Gamma_{\rm min}$ and $q_{\rm extreme}$ are different for each solid curve.) When q drops below $q_{\rm extreme}$ [based on the function $q_{\rm ch}$, this will only happen along curves for which $M_{\rm tot} < (1 + q_{\rm extreme})M_{\rm ch} = 1.85 M_{\odot}$], each curve climbs back above $\Gamma_{\rm min}$, reflecting the fact that Eq. (4.12) admits two solutions over the relevant range of mass ratios. This, in turn, implies that for mass-transferring DWD systems that have $\log(f) < -1.74$, a measurement of $f^{(1)}$ will generate two possible solutions – rather than a unique solution – for the pair of key physical parameters $(M_{\rm tot}, q)$.

Once LISA has measured $f^{(1)}$ as well as f for a given DWD system, Figure 4.3 provides a graphical means of determining the values of $M_{\rm tot}$ and q for the system, assuming it is undergoing a phase of stable CMT. We do not expect that LISA will probe the entire parameter space depicted in this figure, however. As discussed above, we expect that LISA will only be able to detect frequency changes in systems for which $t_{\rm O-C} \lesssim 1$ yr. Using expression (4.3), this means that LISA will only be able to measure $f^{(1)}$ for systems that have,

$$\Gamma \gtrsim 2.57 \times 10^{-5} f^{-8/5} \text{ seconds} \,. \tag{4.18}$$

The dashed black line in Figure 4.3 with a slope of $-8/5$ that is labeled "$t_{\rm O-C} = 1$ year" shows this boundary; the parameter regime that can be effectively probed by LISA lies above and to the right of this line.

5. Bounds on the Existence of DWD Populations in the Amplitude-Frequency Domain*

The previous sections have considered evolving DWD systems with specific system parameters to illustrate population boundaries in LISA's amplitude-frequency domain. We can now extend this to a broader DWD population and apply the same arguments for placing boundaries even on their possible descendents such as Type Ia supernovae. As shown in the top panel of Fig.(5.1), the amplitude-frequency domain for the DWD population is mainly bounded by two curves that are already familiar to us from the previous section. The top boundary (red solid line with positive slope) represents the highest allowable inspiral tranjectory for a $q = 1$ DWD system. It also becomes the limiting inspiralling trajectory for all DWD systems because as mentioned in §1.6, $q \leq 1$. According to Eq. (2.1), this boundary is defined by the expression,

$$\log(rh_{\rm norm}) = 0.731 + \frac{2}{3}\log f \tag{5.1}$$

The curved boundary to the right (solid red line) represents the locus of inspiral termination points for a $q = 1$ system where the donor just fills its Roche lobe and where it is expected that further evolution of the system guides it to lower frequencies due to mass transfer. Again, this curve is the limiting inspiral termination boundary for all DWD systems. In fact, the termination boundaries for lower q systems lie to the left of this curve, as was illustrated in Fig.(4.1). This bounding curve is given approximately by the expression,

$$\begin{aligned} \log(rh_{\rm norm}) \approx 0.703 \;&+\; 0.637\ \log f - 0.017\ (\log f)^2 \\ &+\; 0.298\ (\log f)^3 + 0.061\ (\log f)^4 \end{aligned} \tag{5.2}$$

*Reproduced by permission of the AAS

At low frequencies we can import the $t_{\rm O-C} = 1$ year boundary from Fig.(4.1) whose expression is given in Eq.(4.7). With these three boundaries we can restrict the region occupied by DWD systems that have measurable $\dot{f}$ by LISA in the amplitude-frequency domain.

We can further sub-divide this space to identify specifically the regions that are allowable for DWD systems at different evolutionary stages. We have already recognized the boundary for DWD's in inspiralling stage. For mass-transferring systems, the accretor's limiting mass (the Chandrasekhar mass) allows us to draw a boundary above which no mass-transferring DWD systems can exist. This is represented by the dashed (green) line ($M_{\rm a} = M_{\rm ch}$) in the top panel of Fig.(5.1) and is given approximately by the expression,

$$\begin{aligned} \log(rh_{\rm norm}) \approx 0.761 \quad &+ \quad 1.005 \ \log f + 0.700(\log f)^2 + 0.700(\log f)^3 \\ &+ \quad 0.214(\log f)^4 + 0.023(\log f)^5 \end{aligned} \tag{5.3}$$

This curve divides the DWD space into two regions.

- **Region I :** If LISA observations place a DWD system in this region, then it must be evolving due to gravitational-wave driven inspiral and the evolution is such that the frequency change as a function of time should be measurable within one year. This region is forbidden for mass-transferring systems because they would have to exceed Chandrasekhar's mass limit to exist.

- **Region II :** DWD binaries in this region can either be inspiralling or mass-transferring systems, but all will show a measurable frequency change within one year. The mass transfer can be stable or unstable depending upon q and $M_{\rm tot}$. For example, as mentioned in the introduction, AM CVn systems undergo stable mass transfer and can exist in this region. It is possible that some of the known AM CVn systems may lie at the lower frequency end of the diagram. The trajectories of systems undergoing stable mass transfer will originate at their respective inspiral termination boundary, similar to $q = 1$, and will asymptotically reach the dashed (green) curve.

Unstable systems may not survive to reach this dashed (green) curve because they evolve on a dynamical time scale, which is much smaller than a chirp time scale, and may face a catastrophic ending. It is useful, then, to further sub-divide region II in order to separate stable systems from unstable ones. However, we need to first define the stable and unstable conditions. This actually depends on how the radius of the star and the Roche lobe are reacting to changes in the mass of the donor. This can be represented by the parameters $\zeta_{\rm d}$ and $\zeta_{\rm L}$, where

$$\zeta_d \equiv \frac{\partial \ln R_d}{\partial \ln M_d}\,, \tag{5.4}$$

which specifies how the radius of the donor changes as it loses mass to its companion. Similarly, from Eq. (2.4) one can determine,

$$\zeta_L \equiv \frac{\partial \ln R_L}{\partial \ln M_d} = (1+q)\frac{\partial \ln R_L}{\partial \ln q}\,, \tag{5.5}$$

which measures how the Roche lobe radius changes as the mass of the donor varies, assuming $M_{\rm tot}$ and $J_{\rm orb}$ are held fixed.

Based on these expressions, we can define $\Delta\zeta$ as,

$$\Delta\zeta \equiv (\zeta_d - \zeta_L)\,. \tag{5.6}$$

Fig.(B.1) in Appendix B shows a plot of $\Delta\zeta$ versus q for different values of $M_{\rm tot}$. Systems which have $\Delta\zeta > 0$ are considered to have stable mass transfer and for systems with $\Delta\zeta < 0$ the mass transfer is considered unstable. If we take the locus of all the points which have $\Delta\zeta = 0$, then it is possible to draw another boundary on Fig.(5.1) which we call as "stability curve".

- **Region III :** The bottom panel of Fig(5.1) shows this boundary identified as the (blue) dotted line originating from the dashed line (green). Systems to the right of stability curve undergo unstable mass transfer and the end result probably is a violent phenomena. Systems to the left of the stability curve undergo stable mass transfer and

will continue to evolve to lower frequencies with steady flow of matter from the donor to the accretor. It can be approximated by the expression:

$$\begin{aligned} \log(rh_{\rm norm}) \approx 2.141 &+ 1.686(\log f) \\ &- 0.141(\log f)^2 + 0.007(\log f)^3 \end{aligned} \tag{5.7}$$

- **Region IV :** For stable mass-transferring systems with $M_{\rm tot} \geq M_{\rm ch}$, the accretor's mass will exceed the Chandrasekhar mass limit and this will likely result in a Type Ia supernova explosion. We can confine the progenitors of these systems by identifying the (q, $M_{\rm tot}$) pair for which $M_{\rm tot} = M_{\rm ch}$ along the stability curve. The evolutionary trajectory for this system is shown in the bottom panel of Fig.(5.1) and is indicated by an arrow pointed towards the dashed (green) line. All the systems that have $M_{\rm tot} \geq M_{\rm ch}$ are considered to be progenitors of Type Ia supernovae will lie on or above the region bounded by this trajectory, $M_{\rm a} = M_{\rm ch}$ curve and the stability curve. The expression for this trajectory can be written as:

$$\begin{aligned} \log(rh_{\rm norm}) \approx &- 1.381 - 2.108(\log f) \\ &- 1.394(\log f)^2 - 0.167(\log f)^3 \end{aligned} \tag{5.8}$$

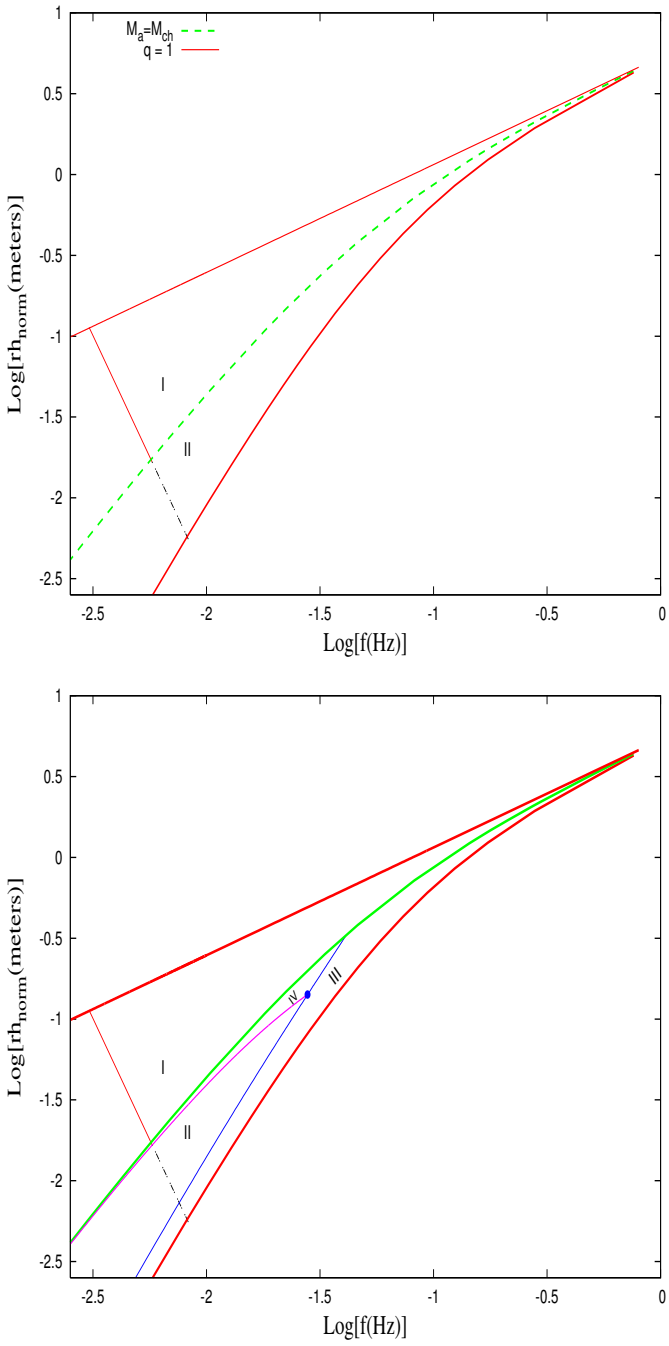

Figure 5.1: DWD population boundaries.

6. Summary

From our current understanding of the structural properties of white dwarfs, it is possible to constrain the space that DWD systems can occupy in the amplitude-frequency domain of *LISA*. Within this space, DWD's have two types of evolutionary mechanisms : (1) Inspiralling systems which evolve through loss of angular momentum due to gravitational radiation (increasing frequency and amplitude) and (2) mass-transfering binaries where one star fills the Roche lobe and transfers mass to its companion (generally decreasing frequency and amplitude). There is a degeneracy in identifying a system in this amplitude-frequency space, if only f and $h_{\rm norm}$ are specified. A measure of the rate of change of frequency ($\dot{f}$) along with the amplitude and frequency of the source will allow us to determine the system's "chirp mass" ($\mathcal{M}$), distance to the source (r)and mainly the physical mechanism governing the evolution. If $\dot{f}$ is positive then the system is inspiralling but if $\dot{f}$ is negative, then the system is in the mass transfer phase. In §4.2, we have outlined how the system parameters like q, $M_{\rm tot}$ and r can be determined in the mass transfer case. These results can also be found in Kopparapu & Tohline (2006).

We also realized that there are both advantages and disadvantages if a non-zero $\dot{f}$ can be measured. The advantage is that (i) the physical mechanism governing the evolution (inspiral or mass transfer) will be known and (ii) it is possible to find the distance r to the source and its chirp mass. The disadvantage is that we need more accurate templates than continous wave templates (constant frequency) to follow the evolution of the system if we want to maintain phase coherence. As shown in Eq.(3.10) and Eq.(3.19), a non-zero $\dot{f}$ can be taken into account with these equations and phase coherence can be maintained for longer time than continous wave templates.

7. Part II : Introduction

The preceding discussion of DWD systems considered in detail the bounds on the population of these systems within the LISA amplitude-frequency domain. In the following sections, we will concentrate more on generating gravitational-wave templates from DWD systems during the mass-transferring phase of their evolution. Especially, we will focus on the systems which are in Region III of Fig.(5.1) and undergo unstable mass transfer. Here, only direct impact systems with comparable masses are studied, meaning the stars are so close to each other that the stream from the donor impacts the accretor directly without forming a disk.

Accurate three-dimensional hydrodynamical simulations are available to predict the strength of the gravitational waves from mass-transferring binaries of this type (D'Souza et al., 2006) but the simulations are inflexible if one wants to generate templates by scaling them to different models of binary systems. It would take a considerable amount of computational time if the parameters of the binary system (for example: masses or initial separation) are changed to simulate a large number of different systems. Moreover, due to constraints on the computational grid, the onset of mass transfer cannot be properly simulated, which is an important piece of information if one wants to depict an entire evolution of mass-transferring binaries. Here we develop a better model than a point mass approximation, but also one which is not as complex as a full non linear hydrodynamical simulation. The objective is to try and reproduce the results of hydrodynamic simulations as accurately as possible without consuming considerable computation time. Also it is worth mentioning that the applicability of our newly developed model is not restricted to systems in Region III of Fig.(5.1); it can also be applied to systems in Region II & IV that are in the stable mass transfer phase.

In Part I of this dissertation, we have used the zero-temperature mass-radius relation for a white dwarf (Eq.(2.3)) which is a close approximation to real white dwarfs. From here

onwards, to simplify things, we will consider that the white dwarf is a "polytrope" and has a simpler equation of state (EOS) (See Appendix C for a review of structural properties of polytropic stars). But we note that a more general or correct treatment is possible by extending the model we have developed. A polytropic relation has pressure proportional to some power of the density of the star. It can be written as

$$P = K\rho^{\gamma} = K\rho^{1+\frac{1}{n}} \tag{7.1}$$

where K is the polytropic constant[11], γ is the polytropic exponent, ρ is the density of the star and n is the polytropic index. For low-mass white dwarf stars, $n = 3/2$, $P = K\rho^{5/3}$. We adopt this value of n throughout our discussion.

The treatment in this part of the dissertation is illustrative, meaning that we are trying to set the stage for generating banks of templates; additional work will be required to use our model as a tool for template-bank generation. The templates that we present here are based on the familiar expression for the time-dependent gravitational-wave strain $h(t)$ that is produced by a point mass binary system in circular orbit that we introduced earlier in Chapter 1. For point-mass binaries in circular orbit, the total angular momentum $J_{\rm tot} = J_{\rm orb}$, so column 2 of Table 1.1 provides the desired prescription for the functions $(rh_{\rm norm})$ and f in terms of three binary system parameters; $M_{\rm tot}$, q, and $J_{\rm tot}$. However, as will be discussed in Chapter 8, the relationship between $J_{\rm tot}$ and $J_{\rm orb}$ becomes much more complex when the spin of the two stars and related "finite-size" effects are taken into account. As a result, it generally will not be possible to find closed-form algebraic expressions for the functions $rh_{\rm norm}$ and f in terms of $M_{\rm tot}$, q, and $J_{\rm tot}$.

As a demonstration, we are going to compare our model results with two specific binary evolutions from hydrodynamic simulations. The initial binary system parameters for these two models are given in Table 7.1. The values in the table are generated using a three-

[11]This K is different than the one defined in Eq.(2.2) which is a combination of chirp mass and Chandrasekhar's mass.

dimensional self-consistent-field (SCF) technique first developed by Hachisu (1986) (see also Hachisu et al., 1986) and adapted by Motl et al. (2002) to generate synchronously rotating binaries in the rotating frame of the system, so that the binaries are at rest in this frame. We will refer to these models as "**Q0.744**" and "**Q0.409**" so that the respective label uniquely identifies that particular binary with the corresponding system parameters given in Table 7.1.

Table 7.1: Initial model parameters from SCF code.

Parameters	**Q0.744**	**Q0.409**
q	0.744	0.409
$M_{\rm tot}$	0.0419	0.0239
$J_{\rm tot}$	2.285×10^{-3}	7.793×10^{-4}
$R_{\rm a}$	0.3543	0.3070
$R_{\rm d}$	0.3319	0.2453
a	0.9638	0.8169
$\Omega_{\rm orb}$	0.2179	0.2112
$J_{\rm orb}$	2.075×10^{-3}	6.964×10^{-4}
$J_{\rm a}$	1.182×10^{-4}	0.640×10^{-4}
$J_{\rm d}$	9.179×10^{-5}	0.189×10^{-4}
$k_{\rm a}^2$	0.179	0.189
$k_{\rm d}^2$	0.213	0.214
$I_{\rm a}$	5.427×10^{-4}	3.031×10^{-4}
$I_{\rm d}$	4.213×10^{-4}	8.969×10^{-5}

8. Finite-Size Effects

Mathematical expressions derived using the point mass approximation will provide reasonably accurate gravitational-wave templates only when the radii R_d and R_a of the donor and the accretor, respectively, are both small compared to the separation, that is, only when $R_d/a \ll 1$ and $R_a/a \ll 1$. When the stars come close to one another in the sense that the radius of at least one of the stars is no longer small compared to a, the time-dependent behavior of various orbital parameters and, in turn, accurate gravitational-wave templates can be determined only by taking into account various "finite-size" effects. These include: The nonradial nature of the gravitational fields of both stars, which arises from the tidal and rotational distortions of their mass distributions; mass-transfer, which begins when one star (the donor) fills its Roche lobe, that is, when $R_d \geq R_L$; angular momentum that is stored in the spin of the two stars, J_d and J_a, and that may be transferred between the orbit and these spins as the system evolves; and the change in the radii (and the associated moments of inertia) of both stars that occurs in response to mass-transfer.

Here we discuss how the point-mass expression for Kepler's third law, Eq.(1.6), and the system's orbital angular momentum, Eq.(1.7) can be modified to account for such finite-size effects.

8.1 Correction to Kepler's Third Law

In general, we define a function $\mathcal{F}(q, g_{\rm i}, n)$ such that,

$$\mathcal{F}(q, g_{\rm i}, n) = \frac{\Omega_{\rm orb}^2 a^3}{G M_{\rm tot}}, \tag{8.1}$$

where, in addition to q and n, the argument $g_{\rm i}$ is the Roche filling factor of a star and can be expressed as

$$g_{\rm i} = \frac{R_{\rm i}}{R_{\rm L}} \tag{8.2}$$

with $i = a,\ d$ for the accretor and donor, respectively, The deviation from the Kepler's law should be reflected in this function through variations in the values of q, $g_{\rm i}$ and n. The filling factor $g_{\rm i}$ can range from $g_{\rm i} = 0$ (when the star is considered as a point mass) to $g_{\rm i} = 1$ (when the star fills its Roche lobe with $R_{\rm L} = R_{\rm i}$). For instance, if both the stars are considered as point masses, then for all n and q, $\mathcal{F}(q, g_{\rm a} = 0, g_{\rm d} = 0, n)$ should be equal to 1 and Eq.(8.1) simply becomes the familiar Kepler's law. But $\mathcal{F}(q, g_{\rm i}, n)$ becomes a more complicated function if either of the $g_{\rm i}$ values deviates from unity. In the case of n, though it can take any value from 0 to ∞, throughout the remainder of our discussion we consider that the stars follow an $n = 3/2$ polytropic equation of state.

It would be helpful if we could find an analytic expression for $\mathcal{F}(q, g_{\rm i}, n)$ which can readily be substituted into Eq.(8.1) to obtain corrected orbital angular velocity. To achieve this, as a first step we draw from the work of Motl (2001), where a three-dimensional SCF model was built assuming the accretor as a point mass object and the donor as an extended star filling its Roche lobe. This means[12] $g_{\rm a} = 0$ and $g_{\rm d} = 1$. A plot of the function $\mathcal{F}(q, g_{\rm i}, n)$ versus q generated from Motl (2001) data is shown in Fig.(8.1).

If the stars are considered as point masses, the resulting curve would be just a straight line parallel to the x-axis at $\mathcal{F} = 1$. But since one of the stars is considered as an extended object, this function deviates from Kepler's law and the amount of deviation depends upon the mass ratio q.

We can fit a curve to this plot and obtain a functional dependence of $\mathcal{F}$ on mass ratio q. Using the least squared method, we get

$$\mathcal{F}(q, 0, 1, 3/2) \ = \ \mathcal{A} + \mathcal{C}\ q^{\mathcal{B}} \tag{8.3}$$

where $\mathcal{A} = 0.990$, $\mathcal{B} = 0.151$ and $\mathcal{C} = 0.021$.

Since our emphasis here is on mass-transferring binaries, henceforth we will use Eq.(8.3)

[12]The more complicated case of when both $g_{\rm a}$ and $g_{\rm d}$ are simultaneously different from zero is not considered in the present discussion.

as the correction factor affecting Kepler's law. For convenience, we will drop the arguments $g_{\rm i}$ and n for the function $\mathcal{F}$ because we assume that both of them have fixed values. Also, as we discuss systems with different q in the following sections, we explicitly indicate that $\mathcal{F}$ is a function of q.

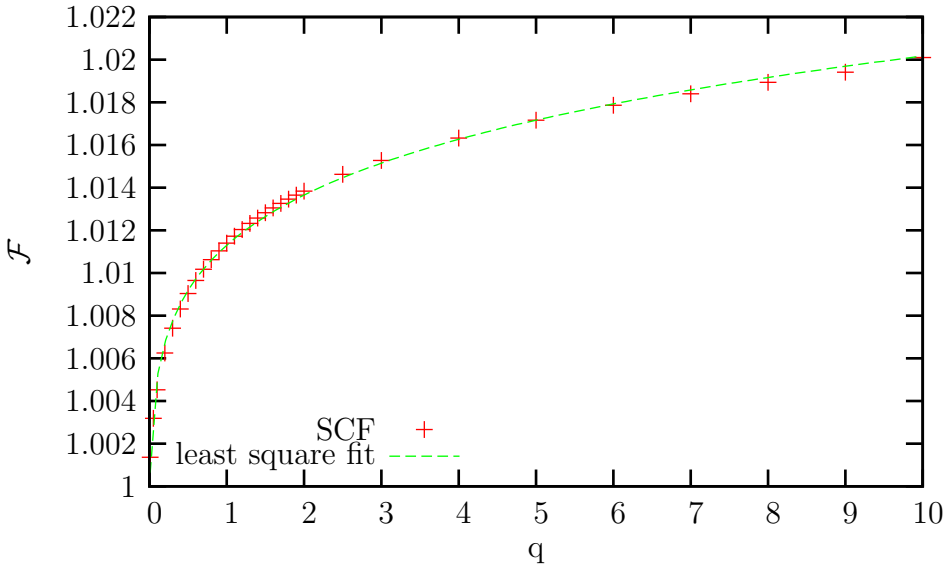

Figure 8.1: Plot of corrected Kepler's law

8.2 Correction to Orbital Angular Momentum

It naturally follows from the above discussion that the orbital angular momentum equation also needs to be corrected because $J_{\rm orb}$ depends on $\Omega_{\rm orb}$. The approximate generalization of Eq.(1.7)

$$J_{\rm orb} \equiv M_{\rm tot} a^2 \Omega_{\rm orb} Q = (G M_{\rm tot}^3 a)^{1/2} \mathcal{F}(q)^{1/2} Q = \left(\frac{G^2 M_{\rm tot}^5}{\Omega_{\rm orb}} \right)^{1/3} \mathcal{F}(q)^{2/3} Q \qquad (8.4)$$

Consequently, both the functions (rh_{norm}) and f, as given in Table 1.1 should reflect a dependence on $\mathcal{F}(q)$. Table 8.1 shows these functional dependencies.

Table 8.1: Expressions for $rh_{\rm norm}$ and f after Kepler correction.

Specify: (1)	$J_{\rm orb}$ (2)	a (3)	$\Omega_{\rm orb}$ (4)
$rh_{\rm norm}$	$\frac{4}{c^4}G^3M_{\rm tot}^5J_{\rm orb}^{-2}Q^3\mathcal{F}(q)^2$	$\frac{4}{c^4}G^2M_{\rm tot}^2a^{-1}Q\mathcal{F}(q)$	$\frac{4}{c^4}(GM_{\rm tot})^{5/3}\left(\mathcal{F}\Omega_{\rm orb}\right)^{2/3}Q$
f	$\frac{1}{\pi}G^2M_{\rm tot}^5J_{\rm orb}^{-3}Q^3\mathcal{F}(q)^2$	$\frac{1}{\pi}(GM_{\rm tot})^{1/2}a^{-3/2}\mathcal{F}(q)^{1/2}$	$\frac{1}{\pi}\Omega_{\rm orb}$

9. Accounting for the Spin of Both Stars

In accounting for the spin of both stars, we must first generalize the expression for the total angular momentum of the binary system to include J_a and J_d. Henceforth, we will adopt an expression for $J_{\rm tot}$ of the form,

$$J_{\rm tot} = J_{\rm orb} + J_a + J_d \,, \tag{9.1}$$

where Eq. (8.4) continues to provide the definition of $J_{\rm orb}$ in terms of the global system parameters [$M_{\rm tot}$, q, and a (or $\Omega_{\rm orb}$)] and, for either one of the stars ($i = a, d$),

$$J_i \equiv I_i \omega_i = k_i^2 M_i R_i^2 \omega_i \,, \tag{9.2}$$

where I_i is the star's moment of inertia about its spin axis, ω_i is the characteristic spin angular velocity of the star, and k_i is the radius of gyration of the star (Claret & Gimenez, 1989).

The appearance of R_i in the expression for J_i most clearly reflects the manner in which the finite size of both stars effects the relationship between $J_{\rm tot}$ and $J_{\rm orb}$. The radius of gyration is a coefficient of order unity whose value is largely dependent on the equation of state of the stellar material and is insensitive to variations in the mass or radius of the star (see Appendix C for details). For the models being developed here, special care will be taken to determine the values of k_d and k_a for each initial binary state taking into account the effects of rotational flattening and tidal elongation, but we will assume that these coefficients are independent of time, even during mass-transfer events.

Obviously, the specification of ω_i is also critical to the determination of J_i and, hence, to the determination of the relationship between $J_{\rm tot}$ and $J_{\rm orb}$. However, in many realistic astrophysical situations — and in all of the evolutionary models under consideration here — the initial value of ω_i, as well as its variation with time, will be fully determined once the

primary binary system parameters have been specified and a physical scenario for the evolution has been prescribed. For all of the systems we will be considering in this investigation, for example, we will assume that the stars are initially synchronously rotating, that is, at time $t = 0$,

$$\omega_d = \omega_a = \Omega_{\rm orb}\,. \tag{9.3}$$

It then becomes advantageous to rewrite Eq. (9.1) in the form (with Kepler correction),

$$J_{\rm tot} \;=\; M_{\rm tot}\biggl\{\Bigl[(GM_{\rm tot})^{2/3}\mathcal{F}(q)^{2/3}Q\Bigr]\Omega_{\rm orb}^{-1/3} + \Bigl[\frac{k_d^2R_d^2\;q + k_a^2R_a^2}{1+q}\Bigr]\Omega_{\rm orb}\biggr\}\,, \tag{9.4}$$

which provides a unique specification of the orbital frequency in terms of the five primary system parameters $[M_{\rm tot},\ q,\ J_{\rm tot},\ R_d,\ R_a]$. Once $\Omega_{\rm orb}$ has been determined numerically from this expression, its value can be used in conjunction with the values of $M_{\rm tot}$ and Q to determine the amplitude $(rh_{\rm norm})$ and frequency f of the gravitational-wave template via the algebraic expressions listed in column 4 of Table 8.1. The orbital separation and orbital angular momentum also can be determined from $\Omega_{\rm orb}$, via expressions (8.1) and (8.4), respectively.

Alternatively, using modified Kepler's law, we can explicitly replace $\Omega_{\rm orb}$ with a in Eq. (9.4) to obtain an expression representing synchronous rotation of the form,

$$J_{\rm tot} \;=\; (GM_{\rm tot}^3a\mathcal{F}(q))^{1/2}\biggl\{Q + \Bigl[\frac{k_d^2R_d^2\;q + k_a^2R_a^2}{a^2(1+q)}\Bigr]\biggr\}\,. \tag{9.5}$$

While it is less obvious how this expression directly relates to the constraint of synchronous rotation because it does not explicitly contain the orbital frequency or the spin frequencies of the stars, in later discussions we will find this expression to be a more advantageous mathematical prescription than Eq. (9.4). We lose nothing by choosing expression (9.5) over Eq. (9.4) because they are mathematically equivalent. Equation (9.5) provides a unique specification of the orbital separation in terms of the five primary system parameters $[M_{\rm tot},\ q,$

$J_{\rm tot}$, R_d, R_a], and once a has been determined numerically from the expression, its value can be used in conjunction with the values of $M_{\rm tot}$ and Q to determine the amplitude ($rh_{\rm norm}$) and frequency f of the gravitational-wave template via the algebraic expressions listed in column 3 of Table 8.1. The orbital angular velocity (that otherwise would have been determined directly from Eq. 9.4) and orbital angular momentum also can be determined from a, via expressions (8.1) and (8.4), respectively.

In an effort to realistically model the time-evolutionary behavior of $\Omega_{\rm orb}$, we will consider two different possible physical scenarios:

- Case I: The stars remain synchronously locked with the (time-varying) orbital angular velocity throughout the evolution.
- Case II: The donor retains its original angular momentum but the accretor robs angular momentum from the orbit as a result of the direct impact of the mass accretion stream on its surface.

Case I is generally thought to apply during the long phase of an inspiral evolution preceding a mass-transfer event when the stars are detached from their Roche lobes; but it may continue to apply throughout a phase of mass transfer if the mass-transfer timescale is sufficiently long. As has been shown by D'Souza et al. (2006), the Case II scenario is reasonable in situations where the rate of mass transfer is high and the accretion stream directly impacts the surface of the accretor.

9.1 Case I Evolutions

For Case I evolutions, Eq. (9.5) serves to define the instantaneous value of the orbital separation at all times, regardless of whether the principal system parameter that is decreasing with time is $J_{\rm tot}$ (due to gravitational radiation) or q (due to mass transfer from the donor

to the accretor). (Alternatively, Eq. 9.4 serves to define the instantaneous value of the orbital frequency at all times.) The initial orbital separation a_0 is determined by evaluating expression (9.5) at time $t = 0$ for a given set of the five primary system parameters [$M_{\rm tot}$, q, $J_{\rm tot}$, R_d, R_a]. Then, if the system evolves because it loses angular momentum via gravitational radiation but the other four primary system parameters remain unchanged, the function $a(t)$ can be determined by letting $J_{\rm tot}$ vary with time as prescribed by Eq. (3.5) and solving Eq. (9.5) numerically for a at various times. If the system evolves because the mass-ratio is dropping from its initial value q_0 as a result of mass transfer, but the other four primary system parameters remain unchanged, the function $a(q)$ will be determined from an expression derived from Eq. (9.5) of the form,

$$\left(\frac{a}{a_0}\right)\left[Q + \frac{k_d^2 R_d^2\ q + k_a^2 R_a^2}{a^2(1+q)}\right]^2 \mathcal{F}(q) \quad = \quad \frac{J_{\rm tot}^2}{G M_{\rm tot}^3 a_0}\,. \tag{9.6}$$

When used in conjunction with the template formulae given in column 3 of Table 8.1, this expression for $a(q)$ will specify the trajectory of Case I evolutions in the amplitude-frequency domain. Then, if the time-dependent behavior of q is prescribed the time-dependent behavior of the amplitude and frequency of the gravitational-wave signal can be determined as well.

9.2 Case II Evolutions

In Case II evolutions, we assume that the stars are initially synchronously rotating so, again, the initial orbital separation a_0 is determined by evaluating expression (9.5) at time $t = 0$ for a given set of the five primary system parameters [$M_{\rm tot}$, q, $J_{\rm tot}$, R_d, R_a]. The system's initial orbital angular momentum $J_{\rm orb,0}$ is then determined by evaluating Eq. (8.4) based on this value of a_0, that is,

$$J_{\rm orb,0} = J_{\rm orb}(t=0) \quad = \quad (G M_{\rm tot}^3 a_0)^{1/2}\left[Q_0 \mathcal{F}(q)^{1/2}\right]. \tag{9.7}$$

Thereafter, the task is to determine how $J_{\rm orb}$ varies with time as the mass-transfer stream extracts angular momentum from the orbit and deposits it onto the accretor. Recalling that

in Case II evolutions both $J_{\rm tot}$ and J_d are assumed to be independent of time, an expression for angular momentum conservation that can be drawn from Eq. (9.1) is, simply,

$$J_{\rm orb} + J_a = \text{constant}\,. \tag{9.8}$$

This, in turn, implies that,

$$\dot{J}_{\rm orb} = -\,\dot{J}_{\rm a}\,, \tag{9.9}$$

where $\dot{J}_a$ is the (generally time-varying) rate at which angular momentum is being deposited onto the accretor by the mass stream.

While a precise determination of $\dot{J}_a(t)$ may not be possible unless detailed hydrodynamic simulations of mass-transfer events are carried out, a reasonable approximation to the function can be constructed by drawing on the work of Verbunt & Rappaport (1988). As matter moves from the L1 Lagrange point toward the accretor, it experiences a torque from the binary system that increases its specific angular momentum (at the expense of the orbit) to a value,

$$j_h \approx (GM_aR_h)^{1/2}\,, \tag{9.10}$$

where R_h is the so-called "circularization radius." According to Verbunt & Rappaport (1988), the ratio of R_h to the binary separation a is only a function of the system mass ratio, q; specifically[13],

$$r_h \equiv \frac{R_h}{a} \approx 0.0883 - 0.04858\log(q) + 0.11489\log^2(q) + 0.020475\log^3(q)\,. \tag{9.11}$$

Roughly speaking, "direct impact" systems (on which we will be focusing here) arise when $R_a \geq R_h$. As the accretion stream strikes the accretor it deposits material onto the accretor

[13]The sign on two terms in this series expression is different from the expression given by Verbunt & Rappaport (1988) because our definition of q is the inverse of theirs.

that carries with it a specific angular momentum given by j_h. Hence,

$$\begin{aligned} \dot{J}_a &= \dot{M}_a\, j_h \approx -\dot{M}_d (G M_{\rm tot} a)^{1/2} \Big[\frac{r_h}{(1+q)}\Big]^{1/2} \\ &= -J_{\rm orb} \Big[\frac{r_h}{q^2(1+q)\mathcal{F}(q)}\Big]^{1/2}\, \dot{q}\,, \end{aligned} \tag{9.12}$$

which, via Eq. (9.9), implies,

$$\frac{d\ln J_{\rm orb}}{dt} = \Big[\frac{r_h}{q^2(1+q)}\Big]^{1/2}\, \frac{dq}{dt}\,. \tag{9.13}$$

Once the (generally time-varying) mass-transfer rate and, hence, $\dot{q}(t)$ is known, Eq. (9.13) can be integrated numerically to give $J_{\rm orb}(t)$. The time-variation of the amplitude ($rh_{\rm norm}$) and frequency (f) of the corresponding gravitational-wave template can then also be determined through the expressions given in column 2 of Table 8.1.

It is interesting to note that, once again, the trajectory of these evolutions in the amplitude-frequency domain can be determined without having to specify the mass-transfer rate. Because time does not appear explicitly on either side of Eq. (9.13) except in the differential operators, the equation can be integrated once to give $J_{\rm orb}$ as a function of q. Specifically,

$$\ln\Big[\frac{J_{\rm orb}(q)}{J_{\rm orb,0}}\Big] = \int_{q_0}^{q} \Big[\frac{r_h}{q^2(1+q)}\Big]^{1/2} dq\,. \tag{9.14}$$

10. Accounting for the Stellar Mass-Radius Relationship

Up to this point in the discussion, we have included the effect of the finite radius of each star in the expression for the star's spin angular momentum. Through the respective moments of inertia of the two stars, the initial choice of R_a and R_d (in combination with a choice of the other three primary system parameters, $M_{\rm tot}$, q, and $J_{\rm tot}$) effect the self-consistent determination of the initial orbital separation through Eq. (9.5). In Case I mass-transfer evolutions, the stellar radii continue to play a direct role in the determination of $a(q)$ through expression (9.6). What we have not previously pointed out, however, is that, in general, the stellar radii will not remain constant during a mass-transfer evolution. As mass is removed from (donor) or added to (accretor) the star, the star will adjust its internal structure on a dynamical time-scale to find a new equilibrium structure which, in general, will have a new equilibrium radius. The time-dependent behavior of the stellar radii must be taken into account when using Eq. (9.6) to solve for the time-dependent orbital separation.

Fortunately, once the equation of state of the stellar material has been specified, it is straightforward to determine how the equilibrium radius of each star will vary with the star's mass. This, in turn, allows the ratio the stellar radii R_a and R_d to their initial values, $R_{a,0} \equiv R_a(t=0)$ and $R_{d,0} \equiv R_d(t=0)$, to be expressed as a known function of the system mass ratio q. For example, a polytrope of index n obeys a mass-radius relationship of the form[14],

$$R = C_n(K) M^{(1-n)/(3-n)} \,. \tag{10.1}$$

(See Appendix C for a review of the structural properties of polytropic stars.)

[14]It is worth noticing that with this simple mass-radius relationship, the parameter $\zeta_{\rm d}$ defined in Eq.(5.4) is just the exponent $(1-n)/(3-n)$. Also, the quantity ζ_* mentioned in Appendix C is exactly the same that can be derived from this mass-radius relation.

Then, if both the donor and accretor are taken to be $n = 3/2$ polytropes, we know that,

$$\frac{R_d}{R_{d,0}} = \left(\frac{M_d}{M_{d,0}}\right)^{-1/3} = \left[\frac{q_0}{(1+q_0)}\frac{(1+q)}{q}\right]^{1/3}; \tag{10.2}$$

$$\frac{R_a}{R_{a,0}} = \left(\frac{M_a}{M_{a,0}}\right)^{-1/3} = \left[\frac{1+q}{1+q_0}\right]^{1/3}. \tag{10.3}$$

With these relations in hand, Eq. (9.6) can be rewritten in the form,

$$\left(\frac{a}{a_0}\right)\Bigg\{Q + k_d^2\left(\frac{a}{a_0}\right)^{-2}\left(\frac{R_{d,0}}{a_0}\right)^2\left[\frac{q}{(1+q)}\right]^{1/3}\left[\frac{q_0}{(1+q_0)}\right]^{2/3} + k_a^2\left(\frac{a}{a_0}\right)^{-2}\left(\frac{R_{a,0}}{a_0}\right)^2\left[\frac{1}{(1+q)}\right]^{1/3}\left[\frac{1}{1+q_0}\right]^{2/3}\Bigg\}^2 \tag{10.4}$$

$$\mathcal{F}(q) \tag{10.5}$$

$$= \frac{J_{\rm tot}^2}{GM_{\rm tot}^3 a_0}, \tag{10.6}$$

where the explicit dependence of the binary separation a on the two (time-varying) stellar radii has been replaced by a more complex dependence on the single time-varying parameter, $q(t)$. For Case I evolutions, this equation can be solved numerically to give $a(q)$ for any choice of the five primary system parameters
$[M_{\rm tot}, q_0, J_{\rm tot}, R_{d,0}, R_{a,0}]$.

10.1 Illustration: Synchronously Rotating, Spherical Polytropes

Consider the case where both stars are assumed to be spherical, $n = 3/2$ polytropes — in which case, the radii of gyration, $k_d = k_a = 0.452$ (see Appendix C) — and where the fluid in both stars has the same specific entropy, *i.e.*, $K_d = K_a$, so the ratio of the initial radii of the stars is fixed by the initial mass ratio q_0 via the expression,

$$\frac{R_{a,0}}{R_{d,0}} = \left(\frac{M_{a,0}}{M_{d,0}}\right)^{-1/3} = q_0^{+1/3}. \tag{10.7}$$

If the binary system follows a Case I evolution, that is, if the stars remain in synchronous rotation with the orbit throughout the evolution, then Eq. (10.4) takes the simpler form,

$$\left(\frac{a}{a_0}\right)\left[Q + A^2\frac{1+q^{1/3}}{(1+q)^{1/3}}\left(\frac{a}{a_0}\right)^{-2}\right]^2 \mathcal{F}(q) = B\,, \tag{10.8}$$

where,

$$A \equiv 0.452\left[\frac{q_0}{1+q_0}\right]^{1/3}\left(\frac{R_{d,0}}{a_0}\right), \tag{10.9}$$

$$B \equiv \frac{J_{\rm tot}^2}{GM_{\rm tot}^3 a_0}\,. \tag{10.10}$$

In the limit $A \ll 1$ — usually this means $(R_{d,0}/a_0) \ll 1$ — Eq. (10.8) reduces to the point mass relation for $a(q)$ that is derivable from Eq. (8.4) with $\mathcal{F} = 1$, namely,

$$a\ Q^2 = \frac{J_{\rm tot}^2}{GM_{\rm tot}^3}\,, \tag{10.11}$$

and it becomes clear how a can be replaced in the template formulae given in column 3 of Table 8.1 to give analytical expressions for $rh_{\rm norm}$ and f that are entirely in terms of only three principal parameters of the binary system $[M_{\rm tot}, q, J_{\rm tot} \approx J_{\rm orb}]$. More generally, however, the initial radius of the donor[15] $R_{d,0}$ must be included among the specified system parameters and Eq. (10.8) has to be solved numerically in order to determine the binary separation initially (because a_0 is in the definition of both A and B), as well as at any later point in time or, equivalently, for all other $q < q_0$.

Realistically, mass-transfer will not begin unless the radius of the donor is initially a sizeable fraction of the binary separation and fills its Roche lobe. That is to say, $R_{d,0}$ should not be specified independently of a_0. Conveniently, Eggleton (1983) has demonstrated that the value of the ratio R_d/a at which the donor marginally fills its Roche lobe is only a function of the mass ratio q. See our earlier Eq.(2.4) Hence, the constants A and B in Eq. (10.8) are

[15]Because we have specified that the polytropic constant in both stars is the same, the initial radius of the accretor is not an independent system parameter. It necessarily has the value given by Eq. (10.7), namely, $R_{a,0} = q_0^{1/3} R_{d,0}$.

both fully determined once the initial mass ratio is specified, as follows:

$$A = 0.452\Big[\frac{q_0}{1+q_0}\Big]^{1/3}\Big[\frac{0.49\ q_0^{2/3}}{0.6\ q_0^{2/3}+\ln(1+q_0^{1/3})}\Big], \tag{10.12}$$

$$B = \Big[Q_0^2 + A^2\frac{1+q_0^{1/3}}{(1+q_0)^{1/3}}\Big]^2. \tag{10.13}$$

Via these two expressions and Eq. (10.8), therefore, the functional dependence of the ratio a/a_0 on q is also fully determined once q_0 is specified. In conjunction with the template formulae given in column 3 of Table 8.1, this is sufficient information to predict the system's evolutionary trajectory in the amplitude-frequency domain.

11. Accounting for Rotational and Tidal Distortions

In binary star systems that undergo mass-transfer, the donor star is, by definition, tidally elongated because it is filling its Roche lobe. If the donor is in synchronous rotation with the orbit, it also will be noticeably rotationally flattened. The accretor may also be noticeably distorted from a sphere if the ratio R_a/a is not small. In our treatment of finite-size effects, these rotational and/or tidal distortions will influence our modelling principally through the effect they have on each star's moment of inertia. Most importantly, they can cause the star's radius of gyration to differ from the value that is readily derived for spherical stars (see Appendix C).

In the model comparisons that we make in chapter 13, for each choice of the initial mass ratio q_0 we rely upon a SCF technique to generate an accurate model of the donor as it fills its Roche lobe (at time $t = 0$). We then draw from this SCF model the initial effective radius of the donor, $R_{d,0}$, as well as the donor's radius of gyration, k_d^2. Because $R_d/a \approx R_L/a$ and, as we discussed earlier, R_L/a is only a function of q, the effect that rotational and tidal distortions have on k_d^2 should only have to be determined once, for each choice of the parameter q. For a given system mass ratio, q, however, the accretor can assume a wide range of initial radii. The ratio R_a/a can be assigned an initial ratio anywhere from near zero (the point mass limit) to of order unity, in which case the accretor also may nearly fill its Roche lobe. For the purposes of generating gravitational-wave templates that span a wide range of the parameter R_a/a, we have developed a numerical tool that can readily determine the radius of gyration of the accretor k_a^2 for arbitrarily specified values of the primary binary system parameters $[M_{\rm tot}, q, J_{\rm tot}, R_d, R_a]$.

11.1 Formulation

Generally, an accretor that is both tidally and rotationally distorted will exhibit an equilibrium mass-density distribution $\rho(\mathbf{x})$ that is distorted in a nontrivial way from the spherical shape that it would otherwise assume in the absence of such distortions. As Chandrasekhar (1933a) has pointed out, however, if the accretor has a polytropic equation of state (as we are assuming here), the distortions can be well-approximated through a perturbation of the density distribution $\rho_{\rm sph}(r)$ that is derived for spherical polytropes from the solution $\theta_n(\xi)$ of the Lane-Emden equation (see Appendix C). Specifically,

$$\rho_{\rm sph}(r) \;=\; \rho_c[\theta_n(\xi)]^n\,, \tag{11.1}$$

where ρ_c is the central density of the accretor,

$$\xi \;\equiv\; \frac{r}{\alpha_n}\,, \tag{11.2}$$

and the characteristic length scale for the polytrope,

$$\alpha_n \equiv \left[\frac{(n+1)K}{8\pi G}\rho_c^{1/n-1}\right]^{1/2}\,. \tag{11.3}$$

where K is the polytropic constant.

At the center of a spherical polytrope, $\theta_n(0) = 1$; and its surface is defined by the dimensionless radius ξ_1 at which the function θ_n first drops to zero[16]. The numerical value of ξ_1 along with other properties of spherical polytropes are given in Appendix C for a range of values of the polytropic index, n.

Following Chandrasekhar (1933c), in the presence of rotational and tidal distortions we define a more general polytropic function,

$$\Theta_n(\xi,\theta,\phi) \;\equiv\; \left[\frac{\rho(r,\theta,\phi)}{\rho_c}\right]^{1/n}\,, \tag{11.4}$$

[16]The polytropic function θ_n has its first zero at ξ_1, but mathematically the function continues on beyond this radius. In order to determine the more general, "perturbed" polytropic function Θ_n shown in Eq. (11.5), θ_n must be evaluated on beyond the surface of the unperturbed configuration to radial locations $\xi > \xi_1$, where θ_n becomes negative. In this region we use Taylor expansion to evaluate θ_n near its first zero.

whose dependence on the spherical coordinates (ξ, θ, ϕ) can be written as a sum of the spherically symmetric polytropic function θ_n (not to be confused with the spherical polar coordinate, θ) and a three-component, "perturbation" of the form[17],

$$\begin{aligned}\Theta_n(\xi,\theta,\phi) &= \theta_n(\xi) + 2(1+q)\mathcal{F}(q)\Big(\frac{\alpha_n\xi_1}{a}\Big)^3\frac{|\theta_1'|}{\xi_1}\cdot \\ &\Big\{\psi_0(\xi) - \frac{5}{6}\,\frac{\xi_1^2 P_2(\cos\theta)\;\psi_2(\xi)}{[3\;\psi_2(\xi_1)+\xi_1\;\psi_2'(\xi_1)]} \\ &+ \frac{q}{(1+q)}\sum_{j=2}^{4}\Big(j+\frac{1}{2}\Big)\Big(\frac{\alpha_n x i_1}{a}\Big)^{j-2}\cdot \\ &\frac{\xi_1^2 P_{\rm j}(\sin\theta\cos\phi)\;\psi_{\rm j}(\xi)}{[(j+1)\;\psi_{\rm j}(\xi_1)+\xi_1\;\psi_{\rm j}'(\xi_1)]}\Big\}. \end{aligned} \tag{11.5}$$

Here the center of the spherical coordinate system is aligned with the center of the accretor, the polar axis ($\theta = 0$) is aligned with the accretor's spin axis, and the radial coordinate line whose orientation is $(\theta, \phi) = (\pi/2, 0)$ points toward the donor along the line adjoining the centers of the two stars. In expression (11.5), P_i are Legendre polynomials; the four radial functions,[18] ψ_0, ψ_2, ψ_3 and ψ_4, have been derived by Chandrasekhar (1933a,b) to provide solutions to the distorted equilibrium force-balance equations; $\psi_j' \equiv d\psi_j/d\xi$; and $\theta_1' = d\theta/d\xi$, evaluated at ξ_1.

In our present analysis, we have focused on $n = 3/2$ polytropes for which the characteristic scale length becomes,

$$\alpha_n = \alpha_{3/2} \equiv \Big[\frac{5K}{8\pi G}\rho_c^{-1/3}\Big]^{1/2}. \tag{11.6}$$

With this in hand, a determination of $\Theta_{3/2}(\xi, \theta, \phi)$ and the three-dimensional, distorted density distribution $\rho(r, \theta, \phi)$ is straightforward if the mass ratio q and the separation a of the binary system are specified along with the polytropic constant K and central density ρ_c of the accretor.

[17]We have written this polytropic function *with* a Kepler correction. The original expression given in Chandrasekhar (1933c) can easily be obtained by substituting $\mathcal{F}(q) = 1$.

[18]Chandrasekhar, in his published analysis, does not include the higher order terms. Here we have derived additional higher-order terms to match the values listed in the appendices of Chandrasekhar (1933a,b). The expanded radial functions with the higher order terms are given in Appendix D of this dissertation.

The radius of gyration for the tidally and rotationally distorted polytrope is also then straightforwardly determined as follows. The mass and the relevant moment of inertia are obtained via the volume integrals,

$$M_\Theta = \rho_c \; \alpha_{3/2}^3 \int (\Theta_{3/2})^{3/2} \xi^2 d\xi \sin(\theta) d\theta d\phi \,, \tag{11.7}$$

and,

$$I_\Theta \;\; = \;\; \rho_c \; \alpha_{3/2}^5 \int (\Theta_{3/2})^{3/2} \xi^4 d\xi \sin(\theta) \; d\theta \; d\phi \,, \tag{11.8}$$

where it is understood that, for each angular direction (θ, ϕ), the integral over ξ is carried from the center of the star ($\xi = 0$) out to the location of the first zero of the function $\Theta_{3/2}$. The radial location $\xi_{\rm eq}$ at which $\rho(\xi, \pi/2, 0)$ first goes to zero defines the equatorial radius of the distorted object via the expression,

$$R_\Theta \;\; = \;\; \alpha_{3/2} \xi_{\rm eq} \,. \tag{11.9}$$

Then the radius of gyration is,

$$k_\Theta^2 \equiv \frac{I_\Theta}{M_\Theta R_\Theta^2} = \frac{\int (\Theta_{3/2})^{3/2} \xi^4 d\xi \sin(\theta) \; d\theta \; d\phi}{\xi_{\rm eq}^2 \int (\Theta_{3/2})^{3/2} \xi^2 d\xi \sin(\theta) d\theta d\phi} \,. \tag{11.10}$$

11.2 Iterative Solution

The formulation that has just been outlined can only be used to determine k_a^2 in our initial binary model if we specify the initial separation a_0 of the binary system. But because a_0 is constrained by the expression,

$$a_0 \Big[Q_0 + \frac{k_d^2 R_d^2 \; q_0 + k_a^2 R_a^2}{a_0^2 (1 + q_0)} \Big]^2 \mathcal{F}(q) \;\; = \;\; \frac{J_{\rm tot}^2}{G M_{\rm tot}^3} \,, \tag{11.11}$$

which has been obtained by evaluating Eq. (9.6) at time $t = 0$, the value of a_0 is not known until the accretor's radius of gyration k_a^2 has been specified. We have therefore found it necessary to iterate between a solution of Eq. (11.11) and an evaluation of Eq. (11.5) in

order to determine k_a^2 and a_0 simultaneously, in a self-consistent fashion. At the same time, it has been necessary to develop a method by which the characteristic polytropic length scale $\alpha_{3/2}$ that appears explicitly in Eq. (11.5) can be specified in terms of our preferred system parameters $[M_{\rm tot}, q_0, R_a]$ instead of in terms of the initial central density ρ_c and the polytropic constant K_a of the accretor, as indicated by expression (11.6). The iterative procedure that has been developed goes as follows:

- The set of five primary system parameters $[M_{\rm tot},\, q_0,\, J_{\rm tot},\, R_d,\, R_a]$ is specified and the values of these parameters remain fixed throughout the iteration.

- The radius of gyration k_d^2 is obtained for the Roche-lobe-filling donor from a solution of the self-consistent-field equations; its value is held fixed throughout the iteration.

- For the first step of the iteration ($i = 1$): A "guess" for k_a^2 is obtained from the value of the radius of gyration for a spherically symmetric, $n = 3/2$ polytrope; and ρ_c, K, and $\alpha_{3/2}$ are set to the values they would have for a spherical polytrope of radius R_a and mass $M_a = M_{\rm tot}/(1+q)$. That is (see Appendix C),

$$k_a^2|^{i=1} = 0.204\,, \tag{11.12}$$

$$\rho_c|^{i=1} = \frac{\xi_1^3}{4\pi m_{3/2}}\left[\frac{M_{\rm tot}}{(1+q)R_a^3}\right], \tag{11.13}$$

$$K_a|^{i=1} = \frac{8\pi G}{5\xi_1}(4\pi m_{3/2})^{-1/3}\left[\frac{M_{\rm tot}^{1/3}R_a}{(1+q)^{1/3}}\right], \tag{11.14}$$

$$\alpha_{3/2}|^{i=1} = \frac{R_a}{\xi_1}\,. \tag{11.15}$$

- **Begin Outer Loop**: Given $k_a^2|^i$ for the $i^{\rm th}$ iteration step, $a_0|^i$ is determined from a solution of Eq. (11.11).

- **Begin Inner Loop**: Given $a_0|^i$ and $\alpha_{3/2}|^i$ for the $i^{\rm th}$ iteration step, $\Theta_{3/2}|^i$ and the location of its first zero in the equatorial plane $\xi_{\rm eq}|^i$ are determined from a solution of Eq. (11.5).

- Given $\alpha_{3/2}|^i$ and $\xi_{\rm eq}|^i$, $R_\Theta|^i$ is determined from Eq. (11.9).

- If $|1-(R_\Theta|^i/R_a)| > \epsilon_R$ — that is, if $R_\Theta|^i \neq R_a$ to within a specified tolerance ϵ_R — the characteristic scale length of the polytrope is adjusted to a value,

$$\alpha_{3/2}|^{i+1} = \alpha_{3/2}|^i \frac{R_a}{R_\Theta|^i}\,,$$

  in an effort to bring the solution in line with the desired radius R_a and the "inner loop" is repeated.

  ElseIf $|1-(R_\Theta|^i/R_a)| \leq \epsilon_R$, **Exit Inner Loop**.

- Given $\Theta_{3/2}|^i$ and $\xi_{\rm eq}|^i$ from the converged "inner loop" iteration, $k^2_\Theta|^i$ is determined from Eq. (11.10).

- If $|1-(k^2_\Theta|^i/k^2_a|^i)| > \epsilon_k$ — that is, if $k^2_\Theta|^i$ is significantly different from the the value of k^2_a that was "guessed" for this iteration step — we set $k^2_a|^{i+1} = k^2_\Theta|^i$ and the "outer loop" is repeated.

  ElseIf $|1-(k^2_\Theta|^i/k^2_a|^i)| \leq \epsilon_k$, **Exit Outer Loop**.

At the end of this double-looped iteration, k^2_a and a_0 have been determined in a self-consistent manner for the specified set of initial binary system parameters [$M_{\rm tot}$, q_0, $J_{\rm tot}$, R_d, R_a]. Simultaneously, the three-dimensional, dimensionless density profile $(\Theta_{3/2})^{3/2}$ and the characteristic scale length $\alpha_{3/2}$ for the distorted polytropic accretor have been self-consistently determined. With this information in hand, the central density of the distorted accretor can be determined from Eq. (11.7) by demanding that $M_\Theta = M_a = M_{\rm tot}/(1+q)$, that is,

$$\rho_c = \frac{M_{\rm tot}}{(1+q)\ \alpha^3_{3/2} \int (\Theta_{3/2})^{3/2} \xi^2 d\xi \sin(\theta) d\theta d\phi}\,, \tag{11.16}$$

and the polytropic constant K_a for the distorted accretor can be determined from Eq. (11.6), that is,

$$K_a \;=\; \frac{8\pi G}{5}\ \alpha^2_{3/2}\ \rho_c^{1/3}\,. \tag{11.17}$$

The distorted density distribution $\rho(r, \theta, \phi)$ is shown as a function of radius in the top and bottom of Fig.(11.1) for models Q0.744 & Q0.409 respectively. The density distribution for a spherical $n = 3/2$ polytrope is also shown for comparison.

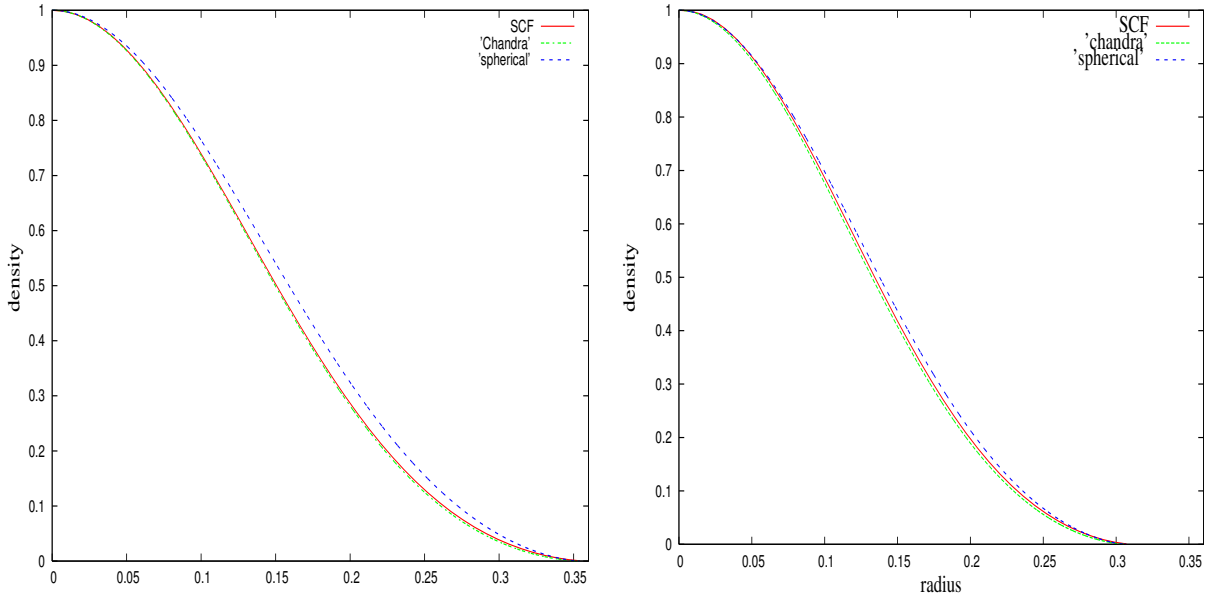

Figure 11.1: Perturbed densities from Chandra's model.

11.3 Results from the Iterative Solution

Tables 11.1 and 11.2 show our converged results for model **Q0.744** before and after we implement Kepler correction. Similarly, Tables 11.3 and 11.4 show the converged results for model **Q0.409** before and after the Kepler correction. All the values are in code units as described in Table.(7.1). The first column in each table represents the model parameters that we are comparing. The second column contains the results obtained from our converged model and the values in third column are obtained from the SCF code. The fourth column represents the percentage difference between the converged model and SCF. The data in the fifth column is obtained when the accretor is considered as a spherical polytrope. The percentage differences in the last column are calculated by comparing the converged model

in the second column with the spherical polytrope model. The errors are significant if the accretor is assumed as a spherical polytrope. But when compared with SCF model on average the differences are in the range of about two or three percent and this might seem not signifcant in terms of comparing the structure of the stars. Since we assume the gravitational waveforms from hydro models as signal from the source, any deviation from these initial values of hydro model will propagate and effects the template accuracy. In other words, phase incoherence between our model and hydro model will arise due to these errors.

Table 11.1: Initial model results for **Q0.744** before Kepler Correction.

	Converged model	SCF	%	Spherical	%
$\rho_{\rm c}$	0.977	1.000	2.2	0.772	26.5
K	3.93×10^{-2}	3.92×10^{-2}	0.3	4.33×10^{-2}	9.2
$I_{\rm a}$	5.44×10^{-4}	5.42×10^{-4}	0.3	9.25×10^{-4}	41.1
$k_{\rm a}^2$	0.1804	0.1799	0.33	0.204	11.5
a_0	0.9864	0.9638	2.3	0.9660	2.1
$\Omega_{\rm orb}$	0.2089	0.2179	4.1	0.2155	3.0
$J_{\rm orb}$	2.083×10^{-3}	2.075×10^{-3}	0.3	2.061×10^{-3}	1.0

Table 11.2: Initial model results for **Q0.744** after Kepler correction.

	Converged model	SCF	%	Spherical	%
$\rho_{\rm c}$	0.990	1.000	0.9	0.772	28.2
K	3.91×10^{-2}	3.92×10^{-2}	0.1	4.33×10^{-2}	9.6
$I_{\rm a}$	5.40×10^{-4}	5.42×10^{-4}	0.3	9.25×10^{-4}	41.6
$k_{\rm a}^2$	0.1792	0.1799	0.34	0.204	12.1
a_0	0.9718	0.9638	0.83	0.9496	2.3
$\Omega_{\rm orb}$	0.2147	0.2179	1.4	0.2223	3.4
$J_{\rm orb}$	2.078×10^{-3}	2.075×10^{-3}	0.1	2.004×10^{-3}	3.6

Table 11.3: Initial model results for **Q0.409** before Kepler correction

	Converged model	SCF	%	Spherical	% difference
$\rho_{\rm c}$	0.981	1.000	1.8	0.838	17.0
K	3.12×10^{-2}	3.12×10^{-2}	0.08	3.34×10^{-2}	6.5
$I_{\rm a}$	3.07×10^{-4}	3.03×10^{-4}	1.3	4.91×10^{-4}	37.4
$k_{\rm a}^2$	0.188	0.189	0.5	0.204	7.8
a_0	0.8411	0.8169	2.9	0.8225	2.2
$\Omega_{\rm orb}$	0.2003	0.2112	5.1	0.2072	3.3
$J_{\rm orb}$	6.977×10^{-4}	6.964×10^{-4}	0.1	6.901×10^{-4}	1.1

Table 11.4: Initial model results for **Q0.409** after Kepler correction.

	Converged model	SCF	%	Spherical	% difference
$\rho_{\rm c}$	0.989	1.000	1.0	0.838	18.0
K	3.11×10^{-2}	3.12×10^{-2}	0.2	3.34×10^{-2}	6.8
$I_{\rm a}$	3.00×10^{-4}	3.03×10^{-4}	0.9	4.91×10^{-4}	38.9
$k_{\rm a}^2$	0.188	0.189	0.5	0.204	7.8
a_0	0.8297	0.8169	1.5	0.8098	2.4
$\Omega_{\rm orb}$	0.2054	0.2112	2.7	0.2130	3.5
$J_{\rm orb}$	6.962×10^{-4}	6.964×10^{-4}	<0.1	6.877×10^{-4}	1.2

12. Analytical Expression for Mass Transfer Rate $\dot{M}_d(t)$

In **Part I**, to obtain the time dependent behavior of the system's mass ratio in mass-transferring systems, we assumed that the mass-transfer rate $\dot{M}_{\rm d}$ was constant throughout the evolution. In real systems, $\dot{M}_{\rm d}$ will vary with time in a complex way and the gravitational waveform will reflect this complex time-variation. Here we draw upon the research of others who have extensively studied mass-transfer events in semi-detached binary systems in order to construct a realistic mathematical prescription for the function $\dot{M}_d(t)$.

12.1 Derivation

The rate $\dot{M}_d$ at which mass is transferred from the donor to the accretor in a semi-detached binary system is, in a very generic sense, governed by the degree to which the radius of the donor star R_d exceeds the Roche lobe radius R_L. As has been discussed in detail by others (Webbink, 1984; Frank et al., 2001), in stars with polytropic atmospheres the mass-transfer rate is expected to be proportional to the fractional radial overflow, $\Delta R/R_d \equiv (R_d - R_L)/R_d$, raised to the $(n + 3/2)$ power, that is,

$$\dot{M}_d \propto \left[\frac{\Delta R}{R_d}\right]^{n+3/2} = -\dot{M}_0\left[1 - \frac{R_L}{R_d}\right]^{n+3/2}, \tag{12.1}$$

where the intrinsically positive proportionality constant $\dot{M}_0$ sets an overall scale for the rate of mass transfer in a particular system. As is described more fully below in §12.2, $\dot{M}_0$ depends on other properties of the binary system that do not vary — or vary only slowly — with time as long as $\Delta R/R_d \ll 1$. Hence, we only need to know how the radius of the donor star and the radius of Roche lobe vary with time in order to obtain a reasonably accurate description of the time-variation of the mass-transfer rate $\dot{M}_d(t)$. It is customary to express

the time-variation of either one of these two characteristic radii (denoted by the subscripts $i = d$ or $i = L$) in the following form:

$$\begin{aligned} \frac{d}{dt}R_i(t, M_d(t)) &= \frac{\partial R_i}{\partial t} + \frac{\partial R_i}{\partial M_d}\dot{M}_d \\ &= R_i\Big[\frac{\partial \ln R_i}{\partial t} + \frac{\partial \ln R_i}{\partial \ln M_d}\frac{\dot{M}_d}{M_d}\Big] \\ &= R_i\Big[\nu_i + \zeta_i\frac{\dot{M}_d}{M_d}\Big]\,, \end{aligned} \tag{12.2}$$

where it is recognized that in addition to any physical processes that might directly cause either radius R_i to change with time, the radii must both change in response to an exchange of mass between the two stars. The latter effect is customarily parameterized in terms of the two dimensionless coefficients, $\zeta_{\rm d}$ and $\zeta_{\rm L}$ defined in Eq.s (5.4) & (5.5), while direct processes are customarily parameterized in terms of the coefficients,

$$\nu_i \equiv \frac{\partial \ln R_i}{\partial t}\,, \tag{12.3}$$

which have units of inverse time. The numerical values of these four coefficients — ν_d, ζ_d, ν_L, and ζ_L — that are appropriate for the models that are of interest to us in this investigation are derived below in §12.2. If we differentiate Eq. (12.1) with respect to time and replace the time derivatives of R_i by the parameterized expressions just derived, we obtain the following first-order, ordinary differential equation that describes the time-variation of $\dot{M}_d$:

$$\begin{aligned} \dot{M}_0^{-1/(n+3/2)}\frac{d}{dt}(-\dot{M}_d)^{1/(n+3/2)} &= \frac{R_L}{R_d}\Big[\frac{d\ln R_d}{dt} - \frac{d\ln R_L}{dt}\Big] \\ &\approx (\nu_d - \nu_L) + (\zeta_d - \zeta_L)\frac{\dot{M}_d}{M_d}\,. \end{aligned} \tag{12.4}$$

The final line of this expression has been obtained by setting $R_L/R_d \approx 1$, which follows from the constraint that $\Delta R/R_d \ll 1$. As Webbink (1984) and Webbink & Iben (1987) have illustrated, for certain values of the polytropic index, Eq. (12.4) is analytically integrable if one assumes that the various parameters (other than $\dot{M}_d$) are independent of time. (As

discussed by Gokhale et al. (2007), this assumption is likely to be valid until the mass ratio of the binary system q has changed significantly from its initial value.) To simplify the derivation, from this point on we will adopt an $n = 3/2$ polytropic index. Then, by defining,

$$y \equiv \left[-\frac{\dot{M}_d}{\mu}\right]^{1/3}, \tag{12.5}$$

$$\mu \equiv M_d\left(\frac{\nu_d - \nu_L}{\zeta_d - \zeta_L}\right), \tag{12.6}$$

and,

$$\tau \equiv \frac{1}{3}\left[\frac{\dot{M}_0}{M_d}(\zeta_d - \zeta_L)(\nu_d - \nu_L)^2\right]^{-1/3}, \tag{12.7}$$

Eq. (12.4) may be written as,

$$\frac{1}{1-y^3}\frac{dy}{dt} = \frac{1}{3\tau}, \tag{12.8}$$

and integrated to give,

$$\frac{t}{\tau} = -\frac{1}{2}\ln\left[\frac{(1-y)^3}{1-y^3}\right] + \sqrt{3}\left[\tan^{-1}\left(\frac{2y+1}{\sqrt{3}}\right) - \frac{\pi}{6}\right]. \tag{12.9}$$

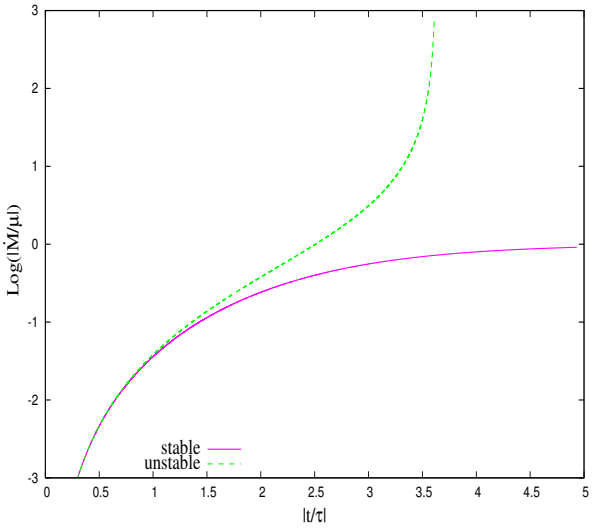

Figure 12.1: Webbink mass transfer rate.

(The term $\pi/6$ inside the last set of brackets is the integration constant required to set $\dot{M}_{\rm d} = 0$ at time $t = 0$.) As Fig. 12.1 illustrates, this expression admits two solutions that

depend on the sign of y, which in turn reflects the sign of the parameter μ. The time t is measured from the onset of mass transfer. For $\zeta_d < \zeta_L$, the mass transfer is dynamically unstable where $\dot{M} \to \infty$ as the time $t \to -2\pi\tau/\sqrt{3}$. This is represented by the dotted line. The solid line is for stable mass transfer ($\zeta_d > \zeta_L$) where $\dot{M}$ approaches $-\mu$ as $t \to \infty$.

It should be noted that the scaling parameters μ and τ depend upon ν_d, ν_L, ζ_d and ζ_L. Since the mass ratio and angular momentum loss due to gravitational-wave radiation (GWR) change from system to system , ζ_L (which depends on mass ratio) and ν_L (which depends on an GWR loss) also change. Consequently μ and τ change from system to system. But this does not affect the shape of the curves shown in Fig(12.1), only the scale on the axes change. In the following sections, we will derive some analytical expressions to find the values of the four quantities influencing μ and τ.

12.2 Evaluation of Time-Independent Parameters

According to Paczynski & Sienkiewicz (1972), if the donor star is a polytrope of index $n = 3/2$, the proportionality constant in Eq. (12.1) is,

$$\dot{M}_0 = 0.215 \frac{G^2 W(q) M_{\rm tot}^2}{K^{3/2}}\,, \tag{12.10}$$

where K is the proportionality constant in the polytropic equation of state,

$$W(q) \equiv q^{1/2}(1+q)^{-2}(1+q^{1/2})^{-4} r_L^{-3}, \tag{12.11}$$

and,

$$r_L \equiv \frac{R_L}{a} \tag{12.12}$$

where $R_{\rm L}$ is defined in Eq.(2.4). For spherically symmetric, $n = 3/2$ polytropes, however, we also know that (Chandrasekhar, 1958),

$$\frac{G^2 M_d}{K^{3/2}} = 3.026 (G\rho_c)^{1/2}\,, \tag{12.13}$$

where ρ_c is the central density of the star. Hence, Eq. (12.10) may be re-written in the form,

$$\dot{M}_0 = 0.6506\frac{(1+q)}{q}W(q)M_{tot}(G\rho_c)^{1/2}\,, \tag{12.14}$$

which can be readily evaluated in terms of the principal parameters of our modelled binary system.

In the case of the four quantities ν_d, ζ_d, ν_L, and ζ_L, we assume that they are not changing with time and some of them are fixed for all values of q because of the equation of state we are assuming for both the stars. To be more specific, depending upon the rate of expansion or contraction of the radius of the donor star, ν_d can be determined for different systems. From the mass-radius relation of a polytrope given in eq.(10.1), it can easily be shown that $\zeta_d = -1/3$ for polytropes with index $n = 3/2$. From the definition of $\zeta_{\rm L}$ in Eq.(5.5) and Eq.(12.12) above , we can write

$$\zeta_{\rm L} = \frac{\partial \ln R_{\rm L}}{\partial \ln M_2} = \frac{\partial \ln a}{\partial \ln M_2} + \frac{\partial \ln r_{\rm L}}{\partial \ln M_2} \tag{12.15}$$

The second term in the above expression can be calculated by differentiating Eq.(2.4) (Marsh et al. (2004) also provides this expression which is exactly the same as ours). Also, the change in the separation (first term) depends on the amount of angular momentum transferred from the stream to the surroundings of the accretor. According to Verbunt & Rappaport (1988), this first term can be written as

$$\frac{d \ln a}{d \ln M_2} = -2\Big[1 - q - \Big((1+q)r_h\Big)^{1/2}\Big] \tag{12.16}$$

where r_h is defined in Eq.(9.11). Combining both terms $\zeta_{\rm L}$ becomes

$$\zeta_L = \frac{(1+q)}{3}\frac{2\ \ln(1+q^{1/3}) - q^{1/3}/(1+q^{1/3})}{0.6q^{2/3} + \ln(1+q^{1/3})} + 2((1+q)r_h)^{1/2} - 2(1-q) \tag{12.17}$$

which is only a function of q.

In case of ν_L, it can be written as

$$\nu_L = \frac{\partial\ \ln R_L}{\partial t} = \frac{\partial\ \ln a}{\partial t} + \frac{\partial\ \ln r_L}{\partial t}$$

from Eq.(12.12) and is true in the absence of mass transfer. Hence, the second term doesnot contribute as it depends only q. Also, from the definition of orbital angular momentum, we can write the change in the separation in terms of $J_{\rm orb}$ as follows

$$\frac{\dot{J}_{\rm orb}}{J_{\rm orb}} = \frac{1}{2}\frac{\dot{a}}{a}$$

Therefore, if we know the angular momentum loss rate from the system, then

$$\nu_L = 2\frac{\dot{J}_{\rm orb}}{J_{\rm orb}}. \tag{12.18}$$

13. Discussion and Results

In Chapter 8-11, we have discussed in detail various finite size effects that come into play to modify the orbital parameters and hence, gravitational-wave signal in DWD binaries; and rotational effects; and in chapter 12 an analytical model was proposed to give the mass transfer rate as a function of various system parameters. In order to generate a template, we have identified that the functions $rh_{\rm norm}$ and f can be determined using the above effects, once we know the initial values of five system parameters $[M_{\rm tot}, q, J_{\rm orb}, R_{\rm d}, R_{\rm a}]$. In this chapter we will illustrate the templates that are generated using the techniques discussed in previous sections by comparing with the results from the hydrodynamic simulations of the two models **Q0.744** and **Q0.409**. In the hydrodynamic models that we are considering, the system is driven by artificially removing angular momentum at a certain rate throughout the evolution to mimic the loss of angular momentum from the system due to gravitational radiation. The adapted rate is different for the two different models. In the following sub-section, we compare the results from our model to hydro simulations and discuss the limitations of our technique.

13.1 Templates for Different Models

As mentioned in Chapter 7, we consider here two models of binary systems : **Q0.744** and **Q0.409**. System parameters that are needed initially to generate the gravitational waveforms have been summarized in Table 7.1. The numerical values of the coefficients $\nu_{\rm d}$, $\nu_{\rm L}$, $\zeta_{\rm d}$ and $\zeta_{\rm L}$ that are suitable for the models we are considering are given in Table 13.1. We set the coefficient $\nu_{\rm d} = 0$ The artificial removal of angular momentum from the system, i.e the imposed 'drag', mentioned above can be incorporated into our models through Eq.(12.18). In the two hydrodynamic models that we have considered, the drag is at a rate of 2% per

orbit ($q = 0.744$) and 1% per orbit ($q = 0.409$). The values of $\nu_{\rm L}$ are then determined by dividing this rate of drag by orbital period for the appropriate model. Also, as explained in §3.2, $\zeta_{\rm d} = -1/3$ because we are assuming the stars are polytropes of index $n = 3/2$ and for a given mass ratio, Eq.(12.17) gives the value of $\zeta_{\rm L}$. With these values we get $\zeta_{\rm d} < \zeta_{\rm L}$ indicating that the mass transfer is dynamically unstable.

Table 13.1: Numerical values of the coefficients.

q	$\nu_{\rm d}$	$\nu_{\rm L}$	$\zeta_{\rm d}$	$\zeta_{\rm L}$	$\nu_{\rm d} - \nu_{\rm L}$	$\zeta_{\rm d} - \zeta_{\rm L}$	$P_{\rm orb}$	drag
0.744	0	-0.001367	-0.333	0.724	0.001367	-1.057	29.26	2%
0.409	0	-0.000653	-0.333	0.0144	0.000653	-0.3474	30.58	1%

These four coefficients are used to determine μ and τ given in Eq.(12.6) and Eq.(12.7) which are used as scaling parameters for the analytical expression describing the mass transfer rate. Since we are attempting to compare our templates with the waveforms from hydrodynamic simulations and since the amplitude and frequency of a gravitational wave depends upon how q is changing with time, it is important that the mass transfer rate predicted from our model closely match with the hydro model. Fig.(13.1) shows the mass tranfer rate as a function of time for the two q values we considered.

The initial part of the hydro evolution looks noisy because of some mass sporadically transferring from the donor to the accretor and due to constraints in the grid resolution, it cannot be resolved. At the time when the hydro model starts evolving (time $t = 0$), there is very little mass transfer between the stars. In the case of the model that we developed, the time $t = 0$ is at the onset of mass transfer. The values of initial mass-transfer rates from these two models donot match because one of them (hydro) has a resolution problem and cannot have an arbitrarily low mass transfer rate and the other one (our model) is a semi-analytical model through which it is possible to have a very low rate of mass transfer when the system first comes into contact. To overcome this problem, we wait until there is appreciable amount of mass transfer in the hydro simulation and match it with the corresponding value of the

mass transfer rate from our model. We assume that the mass transfer rate before this period is so low that the mass ratio q remains constant. Fig.(13.2) shows q as a function of time; we see that the assumption that q remains constant for a while works very well for both models.

Eq.(12.9) shows how the mass transfer rate changes as a function of time. We integrate the mass transfer rate that is given in this equation (the quantity y) to evolve the system and to find $q(t)$. Now that we know the change in q, we substitute it into Eq.(9.14) to find how $J_{\rm orb}$ changes as a function of $q(t)$. These two functions, i.e, $q(t)$ and $J_{\rm orb}(q(t))$, can be used to obtain the gravitational wave amplitude ($rh_{\rm norm}$) and frequency f through column 2 in Table 8.1. Fig's. 13.2, 13.3 and 13.4 show how q, $J_{\rm orb}$ and h_+ (defined in Eq.[1.2]) vary as a function time. The horizontal axis in all the plots is time in the units of initial orbital period of the respective model (given in Table 13.1), so $t^* = t/P_{\rm orb}$.

We can determine the extent to which our model templates are valid by calculating the number of cycles that were in-phase with the waveforms generated from the hydro model. The phase difference $\Delta\phi$, as discussed in chapter 4, is chosen as $\pi/2$ between the models but

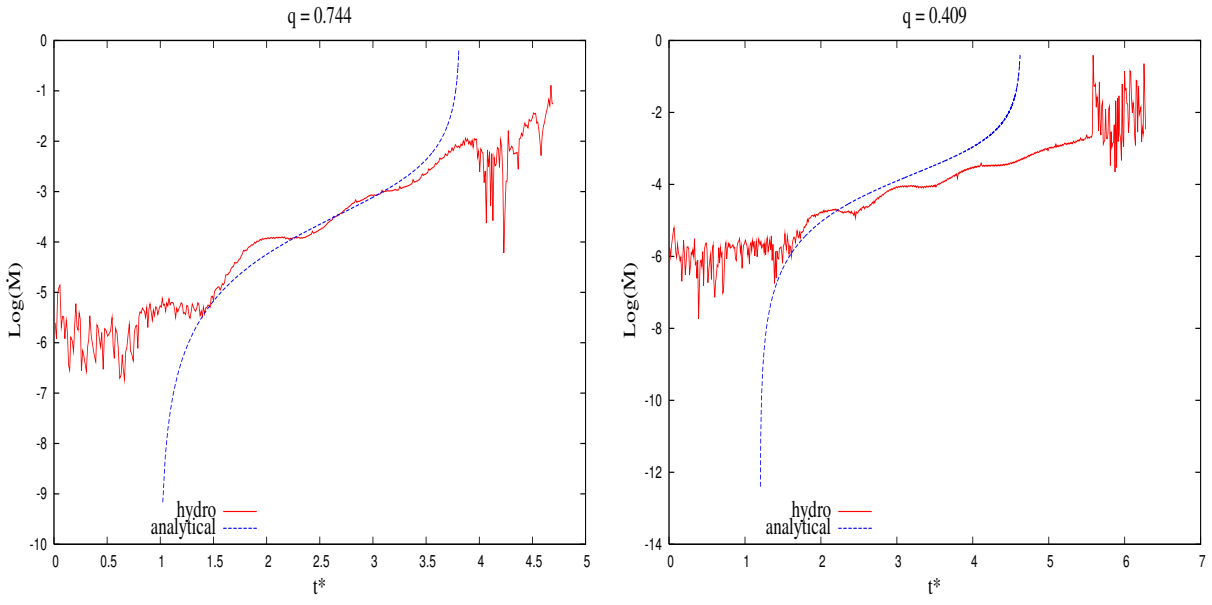

Figure 13.1: Model comparisons of mass transfer rate.

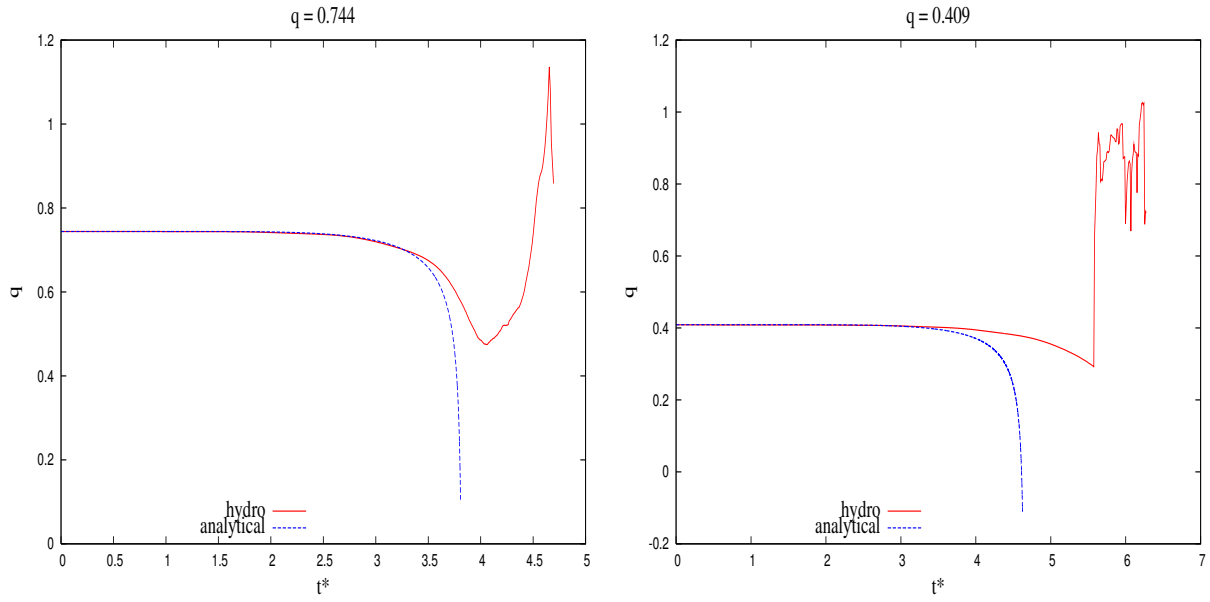

Figure 13.2: Model comparisons of mass ratio.

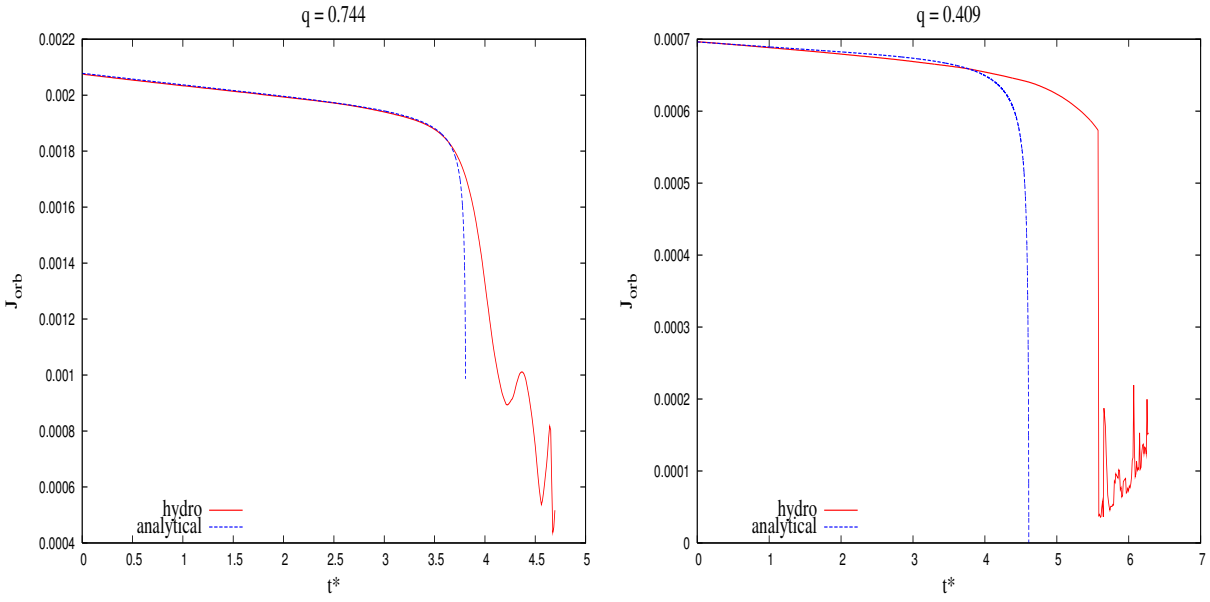

Figure 13.3: Model comparison of orbital angular momentum.

this is arbitrary and one can choose any value for the phase incoherence depending upon the need for accuracy. The phase for the hydro model is calculated by tracking the motion of the center of mass of one of the stars, counting the number of zero-crossings and multiplying it by 2π. For the two illustrative models considered here, **Q0.744** and **Q0.409** , we find that the number of cycles n_{model} that can be matched before there is a phase difference of $\pi/2$ is $n_{model} = 8.4$ for **Q0.744** and $n_{model} = 8$ for **Q0.409**. In the hydro model, the stage at which the donor star is severely disrupted is indicated through the significant reduction in the amplitude. If we disregard this stage and count the number of cycles until this instant, we get $n_{hydro} = 9$ for $q = 0.744$ and $n_{hydro} = 13$ for $q = 0.409$. This means that our model matches the hydro model 93% of the time for **Q0.744** and 61% of the time in **0.409**.

If we guage the success or accuracy of our model with the above method of counting number of cycles that are in phase, then of course it is not reasonable to expect that it matches *exactly* with the hydro model until the end of the evolution. One reason can be determined by looking at the values in Table 13.1. The fact that the coefficients $\nu_{\rm d}, \nu_{\rm L}, \zeta_{\rm d}$ and $\zeta_{\rm L}$ listed in Table (13.1) are only estimates based on analytical expressions from §12 and that they are kept constant throughout the evolution indicates one limit on our model. During the end phase of the evolution where the donor is more distorted and high mass transfer rates are occurring, these coefficients change rapidly from their original values. Since they also determine the scaling factors μ and τ (Eq's 12.6 and 12.7) which in turn affect both the rate of mass transfer and the time at which the system goes unstable (thus affecting the amplitude of the gravitational wave, $h_{\rm norm}$), we see a mismatch during the end phase of the evolution.

Incidentally, it is interesting to note that the scaling parameters μ and τ depend on the difference between the coefficients $\zeta_{\rm d}$, $\zeta_{\rm L}$ and $\nu_{\rm d}$, $\nu_{\rm L}$ rather than the individual values themselves. Therefore, we can reach an estimate of what the values should have been, by

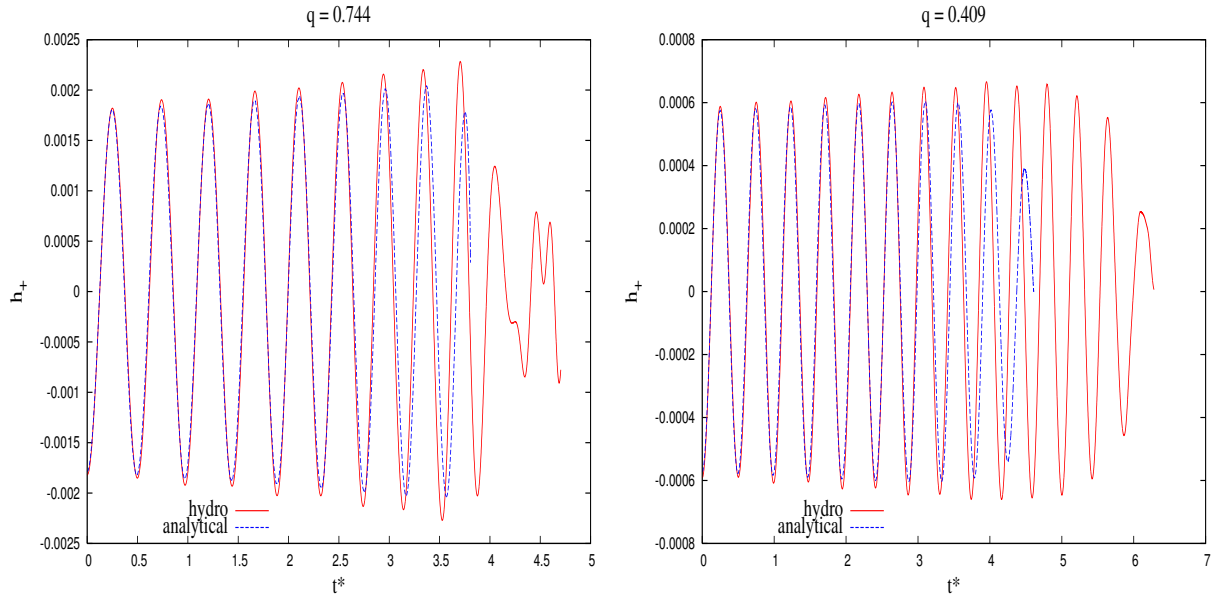

Figure 13.4: Model comparisons of gravitational-wave amplitude.

changing the coefficients, in order to obtain a better mass transfer rate and hence better templates.

14. Conclusions

Double White Dwarf (DWD) systems are considered to be common in our Galaxy as they are believed to be the end products of low-to-intermediate mass main-sequence binary systems, which are quite abundant. They are also guaranteed sources for the proposed space-based gravitational-wave observatory LISA, which is sensitive in the low frequency region of the gravitational wave spectrum. In fact, DWD systems are so numerous that they are expected to form a noise background in the low frequency band of LISA. The path that they traverse across LISA's gravitational-wave "amplitude-frequency" domain is governed by two kinds of evolutions: (1) Inspiralling stage, where the two white dwarfs are detached and inspiral toward each other through loss of angular momentum due to gravitational radiation. During this phase the frequency and amplitude of the emitted gravitational waves keeps increasing ("chirping"). (2) Mass-transfer stage, where they come close enough due to inspiral and the low mass star fills its Roche lobe and starts transferring mass to its companion. During this stage, the stars slowly separate from one another contrary to the case of inspiral, where they approach. This dissertation study was divided into two parts:

Based on the theoretical constraints on the properties of white dwarf stars and their evolution in binary systems, our work for the first time puts restrictions or boundaries on the region of parameter space occupied by the DWD population in LISA's amplitude-frequency domain. From these boundaries, it is possible to identify distinct sub-domains where DWD systems in different evolutionary stages (such as inspiralling, mass transferring) will reside. It is even possible to identify and confine the area of parameter space where progenitors of Type Ia supernova and AM CVn systems can exist. The frequency (and amplitude) of gravitational waves from DWD systems increases slowly when they are in the detached (widely separated) phase and to the first order one can assume them as monochromatic

(constant frequency). When they are close enough, this assumption is no longer valid because the frequency evolution becomes appreciable and higher order terms become important. Based on the operational time for LISA (assumed one year here) another boundary can be set within which a measurement of this frequency evolution should be possible. In fact, it is possible that our conservative assumption of one year time may increase to three or five years, thereby increasing the number of systems that fall within this boundary. It is known that for detached, inspiraling systems, a measurement of the first order change in frequency ($f^{(1)}$) yields binary system parameters such as "chirp mass" (which depends on the masses of the two stars) and distance to the source. Our work shows that for mass-transferring systems a measurement of $f^{(1)}$, $h_{\rm norm}$ and f may reveal the individual components of the masses of DWD binary systems, as well as the distance to each source, but it is more complicated than in the inspiral case.

The boundary plot that confines the DWD population discussed above has a sub-domain (Region III) for mass-transferring systems where the mass transfer between the stars is unstable. The second part of this dissertation has concentrated on generating gravitational-wave templates for the systems which encounter this unstable mass transfer phase. Specifically, direct impact systems (where the stream from the donor *directly* hits the accretor rather than forming an accretion disk) are considered for which three-dimensional hydrodynamic simulations are available. The goal is to develop a model based on approximations to the orbital dynamics of the DWD systems and physics of mass transfer and accurately reproduce the waveforms generated by the hydro dynamical model in considerably less computational time. In this segment of our investigation, white dwarfs are assumed to be $n = 3/2$ polytropes in both hydrodynamic simulations and our model.

Since we are dealing with systems in which the components of the binary system are very close to each other, it becomes necessary to include finite-size of the stars in designing our model. Once the size (radius) of the star is considered, the total angular momentum

equation now must include spin angular momentum of both stars along with the system's orbital angular momentum. However, even orbital angular momentum is affected due to finite-size effects and a correction is applied through a 'modified' Kepler's law. Because the stars are spinning, rotational distortion changes their moment of inertia from the spherical approximation. Tidal effects on each other become important at this stage and this is implemented to generate a better initial model for the system.

To evolve the system from this initial model, we have adopted an analytical mass transfer mechanism from the literature and modified the parameters to be consistent with our present discussion. Two systems were considered here, with $q = 0.744$ and $q = 0.409$, We have generated waveforms for gravitational radiation from these systems and compared with waveforms generated from hydrodynamical simulations. The end result is that our model can match 93% of the evolution for $q = 0.744$ and 61% for $q = 0.409$. During the final stages of the evolution, the donor star is severely distorted in the hydro simulations and the limit on the approximations utilized in our model (finite size of the star, mass transfer rate) is reached at this stage and hence there is a mismatch. The determination of the parameters from the semi-analytical mass transfer model, discussed in Chapter 12, are also partly the reason for this deviation.

What was not discussed in this dissertation is that our model can not only be used during the (stable or unstable) mass transfer regime, but it fits perfectly well to describe the evolution of the system even during the pre-mass-transfer phase, when the systems are detached or just coming into contact. This implies that our model, if carried further, can be used as a tool which can describe the complete evolution of a binary system from its pre-mass-transfer phase to post-mass-transfer period. Of course, as mentioned in Chapter 7, the model developed is only illustrative, setting a stage for the generation of template banks. To acheive this, a more comprehensive parameter space (such as the inclination angle and location of the source in the sky) needs to be taken into account. Also, we have confined

ourselves to a simple equation of state (polytrope) to illustrate the technique developed here. But we can follow the same discussion even for a more realistic white dwarf equation of state. In other words, it is possible to incorporate in our model the mass-radius relationship given in Eq.(2.3) without changing anything significantly.

Bibliography

Anderson, S. F., Haggard, D., Homer, L., Joshi, N. R., Margon, B., Silvestri, N. M., Szkody, P., Wolfe, M. A., Agol, E., Becker, A. C., Henden, A., Hall, P. B., Knapp, G. R., Richmond, M. W., Schneider, D. P., Stinson, G., Barentine, J. C., Brewington, H. J., Brinkman, J., Harvanek, M., Kleinman, S. J., Krzesinski, J., Long, D., Neilsen, E. H. Jr., Nitta, A., & Snedden, S. A. 2005, *Astronomical Journal*, 130, 2230

Abbott B., et al. 2005, Phys. Rev. D, 72, 8.

Andronov, I. L. & Yavorskij, Yu. B. 1990, Contr. Astron. Obs. Skalnate Pleso, 20, 155.

Bender P. L. et al., *LISA Pre-Phase A Report*, 1998.
http://lisa.gsfc.nasa.gov/Documentation/ppa2.08.pdf

Bessell, M. S. 1978, *Proc. Astron. Soc. Aust.*, 3, 220

Branch, D., Tammann, G.A. 1992, Ann. Rev. Astron. Astrophys., 30, 359

Branch, D., Livio, M., Yungelson, L.R., Boffi, F.R., Baron, E. 1995, PASP, 107,1019

Chandrasekhar, S. 1931, ApJ, 74, 81

Chandrasekhar, S. 1933a, MNRAS, 93, 390.

Chandrasekhar, S. 1933b, MNRAS, 93, 449.

Chandrasekhar, S. 1933c, MNRAS, 93, 462.

Chandrasekhar, S. 1958, *An Introduction to the Study of Stellar Structure* (New York; Dover Publications)

Claret, A. & Giminez, A. 1989, Astronomy and Astrophysics Supplement Series, 81, 37.

Cornish N.J. & Larson S.L. 2003, Phys. Rev. D, 10, 103001

Cropper, M., Harrop-Allin, M, K., Mason, K. O., Mittaz, J. P. D., Potter, S. B.,& Ramsay, G. 1998, MNRAS, 293, L57

D'Souza, M., Motl, P., Tohline, J. & Frank, J. 2006, ApJ, 643, 381

D'Souza, M., 2006, Ph.D Dissertation, Louisiana State University, in progress.

Eggleton, P. P. 1983, ApJ, 268, 368

Evans, C. R., Iben, I. Jr. and Smarr, L. 1987, ApJ, 323, 129

Faller, J. E., & Bender, P. L. 1984, in *Precision Measurement and Fundamental Constants II*, ed. B. N. Taylor & W. D. Phillips (NBS Spec. Pub. 617)

Finn, L.S., & Chernoff, D.E. 1993, Phys. Rev. D, 47, 2198

Fowler, R. H. 1926, MNRAS, 87, 114

Frank, J., King, A. R., & Raine, D. J. 2002, *Accretion Power in Astrophysics* (3^{rd} ed; Cambridge: Cambridge Univ. Press)

Gokhale, V., Peng, X., & Frank, J. 2006, *ApJ*, in press

Hachisu, I. 1986, ApJS, 62, 461

Hachisu, I., Eriguchi, Y., & Nomoto, K. 1986, ApJ, 311, 214

Hils, D., Bender, P.L., & Webbink, R.F. 1990, ApJ, 360, 75

Hulse, R. A., Taylor, J. H. 1975, ApJ, 195L, 51

Iben, I., Jr., Tutukov, A. V. 1984, ApJS, 54, 335

Iben, I., Jr., & Tutukov, A. V. 1986, ApJ, 311, 753

Kopparapu, R. K., & Tohline, J. E. 2007, *ApJ*, in press

Liebert, J. 1980, Ann. Rev. Astron. Astrophys., 18, 363

Marsh T. R., Nelemans, G. & Steeghs, D. 2004, MNRAS, 350, 113

Misner, iC. W., Thorne, K. S., & Wheeler, J. A. 1973, *Gravitation* (San Francisco; Freeman & Co.,)

Motl, P. M. 2001, Ph.D. Dissertation, Louisiana State University.

Motl, P. M., Tohline, J. E., & Frank, J. 2002, ApJS, 138, 121

Marsh, T. R., & Steeghs, D. 2002, MNRAS, 331, L7

Napiwotzki, R., Yungelson, L., Nelemans, G., Marsh, T. R., Leibundgut, B., Renzini, R., Homeier, D., Koester, D., Moehler, S., Christlieb, N., Reimers, D., Drechsel, H., Heber, U., Karl, C., & Pauli, E.-M. 2004, ASPC, 318, 402

Nauenberg, M. 1972, ApJ, 175, 417

Nelemans, G., Verbunt, F., Yungelson, L. R. & Portegies-Zwart, S. F. 2000, A& A, 360, 1011

Nelemans, G., Portegies-Zwart, S. F., Verbunt, F. & Yungelson, L. R. 2001 A& A, 368, 939N

Nelemans, G. 2005, PASP, 330, 27

Nelemans, G., Napiwotzki, R., Karl, C., Marsh, T. R., Voss, B., Roelofs, G., Izzard, R. G., Montgomery, M., Reerink, T., Christlieb, N., & Reimers, D. 2005, A&A, 440, 1087

New, K., Centrella, J. & Tohline, J. E. 2000, Phys. Rev. D, 62, 6.

Paczyński, B. 1967, Acta. Astr., 17, 287

Paczynski B.& Sienkiewicz R. 1972, Acta Astr., 22, 73

Peters, P.C., & Mathews, J. 1963, Phys. Rev., 131, 435

Roelofs, G. H. A., Groot, P. J., Marsh, T. R., Steeghs, D., Barros, S. C. C., & Nelemans, G. 2005, MNRAS, 361, 487

Seto, N. 2002, MNRAS, 333, 469

Schutz, B. 1986, Nature, 323, 310

Shu, F. 1982, *The Physical Universe*, New York, University Science Books.

Stroeer, A., Vecchio, A. & Nelemans, G. 2005, ApJ, 633L, 33

Thorne, K.S. 1987, in *300 Years of Gravitation*, ed. S. Hawking & W. Israel (Cambridge: Cambridge University Press), 330-458

Tout, C. A. 2005, ASPC, 330, 279

Verbunt, F. & Rappaport, S. 1988, ApJ, 332, 193

Webbink, R. F. 1984, ApJ, 277, 355

Webbink, R. F., & Iben, I., Jr. 1987, Proceedings of the 2^{nd} Conference on Faint Blue Stars, Schenectady, NY, Davis Press, Inc.

Wu, K., Cropper, M., Ramsay, G., & Sekiguchi, K. 2002, MNRAS, 331, 221

Appendix A

Expressions for Gravitational Wave Strain.

In general, in the weak field approximation, the plus polarization h_+ of the gravitational wave strain for an observer looking down the $z = x_3$ axis of an Euclidean coordinate system, is given by the expression (New et al. (2000))

$$h_+ = \frac{G}{rc^4}(\ddot{\Im}_{xx} - \ddot{\Im}_{yy})\,, \tag{A.1}$$

where $\Im_{ij}$ is the reduced quadrupole moment tensor (Misner et al., 1973) given by

$$\Im_{ij} = I_{ij} - \frac{1}{3}\delta_{ij}\sum_{k=1}^{3} I_k^k\,, \tag{A.2}$$

and, by definition, the second moment of mass distribution is,

$$I_{ij} \equiv \int \rho(r) x_i x_j\,. \tag{A.3}$$

For a point mass binary system in circular orbit that is oriented such that its orbital angular momentum vector aligns with the z-axis of the coordinate system,

$$\Im_{xx} = \frac{M_1 M_2 a^2}{(M_1 + M_2)}\sin^2\phi\,, \tag{A.4}$$

and,

$$\Im_{yy} = \frac{M_1 M_2 a^2}{(M_1 + M_2)}\cos^2\phi\,, \tag{A.5}$$

where, $\phi \equiv \tan^{-1}(y/x)$.

So

$$h_+ = \frac{G}{rc^4}\ \frac{4\dot{\phi}^2 M_1 M_2 a^2}{(M_1 + M_2)}\cos 2\dot{\phi}t \tag{A.6}$$

where $\dot{\phi} = \Omega_{\rm orb}$ is the angular frequency of the circular orbit.

Appendix B

Determining the $\Delta\zeta$ Parameter

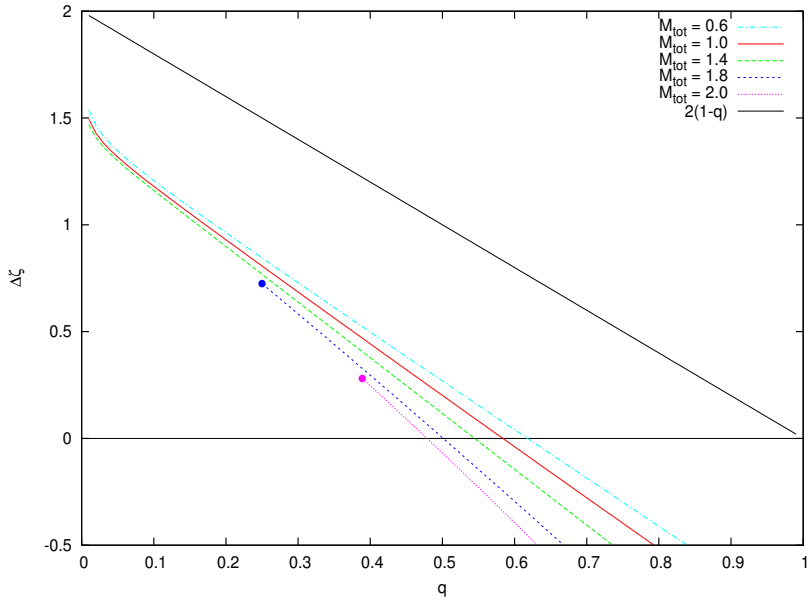

Figure B.1: $\Delta\zeta$ as a function of q.

To obtain a quantitative expression for the mass-transfer rate μ introduced in Eq. (3.11) and, hence, the mass-transfer timescale $\tau_{\rm mt}$, we turn to the discussions of mass-transferring binary systems presented by Webbink & Iben (1987) and Marsh et al. (2004). As these authors have explained, in semi-detached binary systems the mass-transfer rate is determined by the extent to which the radius of the donor star, R_d, exceeds its Roche lobe radius, R_L, and on the degree to which these two radii vary as mass is exchanged between the two stars and as angular momentum is simultaneously lost from the system due to gravitational radiation. Mathematical expressions for all of the relevant parameter variations can be obtained from physical relations that have been presented earlier, in the main body of this dissertation. Directly from the mass-radius relationship for white dwarfs given in Eq. (2.3), for example, one can determine $\zeta_{\rm d}$ and $\zeta_{\rm L}$ from Eq.s (5.4) and (5.5). Finally, from a combination of

Table B.1: Selected values of $q_{\rm crit}(M_{\rm tot})$

$M_{\rm tot}$	$q_{\rm crit}$
0.6	0.61
1.0	0.58
1.4	0.54
1.8	0.50
2.0	0.47

Eq. (2.4) and Eq. (3.8), one can deduce that,

$$\frac{\partial \ln R_L}{\partial t} = \Big(\frac{\partial \ln R_L}{\partial \ln J_{\rm orb}}\Big)\frac{\partial \ln J_{\rm orb}}{\partial t} = -\frac{1}{4\tau_{\rm chirp}}\,. \tag{B.1}$$

In the case of stable CMT, Webbink & Iben (1987) show that μ can be written in a form that depends on variations in R_d and R_L as follows,

$$\mu = -M_d\Big(\frac{\partial \ln R_L}{\partial t}\Big)\frac{1}{(\zeta_d - \zeta_L)} = \frac{q_0}{(1+q_0)}M_{\rm tot}\Big[\frac{1}{4\tau_{\rm chirp}\Delta\zeta}\Big]\,, \tag{B.2}$$

As Figure B.1 shows, $\Delta\zeta$ is positive and $|\Delta\zeta| \sim 1$ for DWD binaries having a wide range of $M_{\rm tot}$ and q. (The implications of a negative $\Delta\zeta$ are discussed in Chapter 5 of this dissertation.) Combining this expression with Eq. (3.13), we deduce that the timescale governing the evolution of semi-detached DWD binaries that are undergoing a phase of stable CMT is,

$$\tau_{\rm mt} \approx \Big(\frac{4\Delta\zeta}{q_0}\Big)\tau_{\rm chirp}\,. \tag{B.3}$$

If $\Delta\zeta$ is negative, however, the system will enter a phase of unstable mass transfer and a significant amount of mass will be transferred from the donor to the accretor on a dynamical time scale. Employing the Eq. (2.3) mass-radius relationship and the $R_L(q)$ relationship defined by Eq. (2.4), Figure B.1 shows how $\Delta\zeta$ behaves as a function of q for various values of $M_{\rm tot}$. If we define $q_{\rm crit}$ as the value of the system mass ratio at which $\Delta\zeta$ crosses zero, we see that $q_{\rm crit}$ is a function of $M_{\rm tot}$. Table B.1 lists the values of $q_{\rm crit}$ that correspond to the five separate values of $M_{\rm tot}$ used in Figure B.1. (As can be deduced from Eq. E.8 in Appendix E, the somewhat simpler model used by Paczyński (1967) gives $q_{\rm crit} = 2/3$, independent of $M_{\rm tot}$.)

Appendix C

Properties of Spherical Polytropes

At each radial location,

$$r \equiv \alpha_n \xi \,, \tag{C.1}$$

within a spherically symmetric polytrope, the "polytropic temperature"

$$\theta(\xi) \equiv (\rho/\rho_c)^{1/n} \,, \tag{C.2}$$

is determined by solving the second-order, ordinary differential equation referred to as the Lane-Emden equation, namely,

$$\frac{1}{\xi^2}\frac{d}{d\xi}\left[\xi^2 \frac{d\theta}{d\xi}\right] = -\theta^n \,, \tag{C.3}$$

where,

$$\alpha_n \equiv \left[\frac{(n+1)K}{4\pi G}\rho_c^{(1-n)/n}\right]^{1/2} , \tag{C.4}$$

and ρ_c is the star's central density, subject to the boundary conditions $\theta = 1$ and $d\theta/d\xi = 0$ at $\xi = 0$. The run of density through the star can then be determined by inverting Eq. (C.2), that is,

$$\rho(\xi) = \rho_c[\theta(\xi)]^n \,, \tag{C.5}$$

and the radius of the star $R = \xi_1 \alpha_n$ is determined by the value of $\xi = \xi_1$ at which the function $\theta(\xi)$ first goes to zero. Two key global parameters of interest to us here are the star's mass,

$$M_* = 4\pi\rho_c\alpha_n^3 \int_0^{\xi_1} \theta^n \xi^2 d\xi = 4\pi\rho_c\alpha_n^3 m_n \,, \tag{C.6}$$

and the star's principal moment of inertia,

$$I_* = \frac{8\pi}{3}\rho_c\alpha_n^5 \int_0^{\xi_1} \theta^n \xi^4 d\xi, \,. \tag{C.7}$$

From these expressions, in turn, we find the following mass-radius relationship for spherical polytropic stars,

$$R_*^{(3-n)} = C_n M_*^{(1-n)} \,, \tag{C.8}$$

where,

$$C_n \equiv (4\pi m_n)^{n-1}\xi_1^{3-n}\left[\frac{(n+1)K}{4\pi G}\right]^n, \tag{C.9}$$

that is,

$$\zeta_* \equiv \frac{\partial \ln R_*}{\partial \ln M_*}\Big|_K = \frac{(1-n)}{(3-n)}. \tag{C.10}$$

We also find that the radius of gyration[1] is,

$$k_*^2 \equiv \frac{I_*}{M_* R_*^2} = \frac{2}{3\xi_1^2}\,\frac{\int_0^{\xi_1}\theta^n\xi^4 d\xi}{\int_0^{\xi_1}\theta^n\xi^2 d\xi}. \tag{C.11}$$

Table C.1 shows numerical values of various quantities for different polytropic indices. Here ζ_* is actually $\zeta_{\rm d}$ and is defined in Eq.5.4.

Table C.1: Numerical values of different polytropic models.

n	ξ_1	$\rho_c/\rho_{\rm mean}$	m_n	ζ_*	k_*^2
0	2.4494	1.0	4.8987	0.3333	0.40
0.5	2.7527	1.8351	3.7879	0.2	0.3259
1.0	3.1416	3.2898	3.1410	0	0.2613
1.5	3.6538	5.9908	2.7136	-0.3333	0.2045
2.0	4.3530	11.403	2.4106	-1.0	0.1548
2.5	5.3555	23.409	2.1868	-3.0	0.1117
3.0	6.8973	54.194	2.0179	$-\infty$	0.0753
3.5	9.5367	152.93	1.8903	5	0.04554
4.0	14.973	622.70	1.7970	3	0.02257
4.5	31.846	6195.54	1.7376	2.3333	0.006892

[1]For a non-rotating spherical polytrope of polytropic index $n = 1.5$, the factor k^2 has the value 0.204 (Andronov & Yavorskij (1990)). This cited paper gives the factors for various polytropic indices.

Appendix D

Chandrasekhar's Radial Functions with Higher Order Terms

We have derived higher order terms for the four radial functions describing Chandrasekhar's distorted density distribution. These functions are written in a concise power series format and the individual terms for each function are tabulated below them. In general, the series can be summed to infinity but we have truncated the series at ten terms ($j = 10$). The big table has the coefficients of each power of ξ and the small table has the denominator values, $d_{\rm i}$, for the respective functions.

$$\psi_0 = \frac{1}{6}\xi^2 + \sum_{j=2}^{\infty} n\xi^{2j} \frac{\sum_{i=0}^{j-2} c_i n^i}{d_{2j}} \tag{D.1}$$

$$= \xi^2\left(\frac{1}{6} + \sum_{j=2}^{\infty} n\xi^{2(j-1)} \frac{\sum_{i=0}^{j-2} c_i n^i}{d_{2j}}\right) \tag{D.2}$$

$$\psi_2 = \xi^2\left(1 + \sum_{j=2}^{\infty} n\xi^{2(j-1)} \frac{\sum_{i=0}^{j-2} c_i n^i}{d_{2j}}\right) \tag{D.3}$$

$$\psi_3 = \xi^3\left(1 + \sum_{j=2}^{\infty} n\xi^{2(j-1)} \frac{\sum_{i=0}^{j-2} c_i n^i}{d_{2j+1}}\right) \tag{D.4}$$

$$\psi_4 = \xi^4\left(1 + \sum_{j=2}^{\infty} n\xi^{2(j-1)} \frac{\sum_{i=0}^{j-2} c_i n^i}{d_{2(j+1)}}\right) \tag{D.5}$$

Table D.1: Coefficients c_i for ψ_0

i	ξ^4	ξ^6	ξ^8	ξ^{10}	$\xi^{12} \times 10^6$	$\xi^{14} \times 10^8$	$\xi^{16} \times 10^{10}$	$\xi^{18} \times 10^{12}$	$\xi^{20} \times 10^{14}$
0	1	-10	70	-4200	0.693	-1.2612	0.4414	-1.8010	0.5133
1	-	13	-157	12730	-2.5881	0.5531	-2.2079	10.0716	-31.6350
2	-	-	90	-13193	3.7224	-9.9673	4.7237	-24.7606	87.4285
3	-	-	-	4678	-2.4439	9.2224	-5.5331	34.6929	141.5288
4	-	-	-	-	0.6168	-4.3750	3.7375	29.8888	146.6579
5	-	-	-	-	-	0.8492	-1.3777	15.8071	99.4816
6	-	-	-	-	-	-	0.2160	4.7426	43.0666
7	-	-	-	-	-	-	-	0.6214	10.8598
8	-	-	-	-	-	-	-	-	1.2191

Table D.2: Denominator values for ψ_0

j	$d_{2\mathrm{j}}$
2	-120
3	15120
4	-1.0886 $\times 10^6$
5	5.9875 $\times 10^8$
6	-84.0647 $\times 10^{10}$
7	12.3575 $\times 10^{14}$
8	-33.6124 $\times 10^{16}$
9	10.3459 $\times 10^{20}$
10	-217.2642 $\times 10^{22}$

Table D.3: Coefficients c_i for ψ_2

i	ξ^4	ξ^6	ξ^8	ξ^{10}	$\xi^{12} \times 10^7$	$\xi^{14} \times 10^9$	$\xi^{16} \times 10^{11}$	$\xi^{18} \times 10^{13}$
0	1	-7	210	- 2310	1.2612	-0.3153	0.3216	-2.1387
1	-	10	-503	7371	-4.9161	1.4348	-1.6619	12.3150
2	-	-	308	-8038	7.3732	-2.6798	0.3669	-31.1440
3	-	-	-	2992	-5.0382	2.5657	-4.4292	44.8276
4	-	-	-	-	1.3203	-1.2570	3.0780	-39.6157
5	-	-	-	-	-	0.2515	-1.1653	21.4601
6	-	-	-	-	-	-	0.1874	-6.5860
7	-	-	-	-	-	-	-	0.8817

Table D.4: Denominator values for ψ_2

j	d_{2j}
2	-14
3	1512
4	-4.9896 $\times 10^5$
5	5.1891 $\times 10^7$
6	-2.4518 $\times 10^{12}$
7	5.0018 $\times 10^{14}$
8	-3.9914 $\times 10^{17}$
9	2.0117 $\times 10^{21}$
10	-2.7483 $\times 10^{25}$

Table D.5: Coefficients c_i for ψ_3

c_i	ξ^5	ξ^7	ξ^9	ξ^{11}	$\xi^{13} \times 10^6$	$\xi^{15} \times 10^8$	$\xi^{17} \times 10^{12}$	$\xi^{19} \times 10^{14}$
0	1	-3	330	-30030	1.8018	-4.5945	0.1222	-3.2937
1	-	4	-749	91633	-6.7578	20.2103	-0.6125	18.4475
2	-	-	434	- 95450	9.7438	-36.4592	1.3112	-45.3577
3	-	-	-	33952	- 6.4022	33.7213	-1.5344	63.4744
4	-	-	-	-	1.6147	-15.9690	1.0342	-54.5558
5	-	-	-	-	-	3.0912	-0.3800	28.7585
6	-	-	-	-	-	-	0.0593	-8.5943
7	-	-	-	-	-	-	-	1.1212

Table D.6: Denominator values for ψ_3

j	d_{2j+1}
2	-18
3	792
4	-9.2664 $\times 10^5$
5	7.7837 $\times 10^8$
6	-3.9697 $\times 10^{11}$
7	8.1458 $\times 10^{14}$
8	-1.6764 $\times 10^{18}$
9	3.3930 $\times 10^{22}$
10	-1.3741 $\times 10^{26}$

Table D.7: Coefficients c_i for ψ_4

c_i	ξ^6	ξ^8	ξ^{10}	ξ^{12}	$\xi^{14} \times 10^7$	$\xi^{16} \times 10^9$	$\xi^{18} \times 10^{11}$	$\xi^{20} \times 10^{15}$
0	1	-11	1430	-50050	3.0630	-2.9099	13.4437	-1.0822
1	-	14	-3129	148125	-11.1889	12.5047	-65.9860	5.9469
2	-	-	1744	-149386	15.6900	-22.0120	138.1769	-14.3338
3	-	-	-	51416	- 10.0202	19.8547	-158.1027	19.6544
4	-	-	-	-	2.4563	-9.1685	104.1801	-16.5491
5	-	-	-	-	-	1.7310	-37.4303	85.4659
6	-	-	-	-	-	-	5.7182	-2.5027
7	-	-	-	-	-	-	-	0.3200

Table D.8: Denominator values for ψ_4

j	$d_{2(j+1)}$
2	-22
3	3432
4	-4.6332 $\times 10^6$
5	1.4702 $\times 10^9$
6	-7.5424 $\times 10^{12}$
7	5.7021 $\times 10^{15}$
8	-2.0196 $\times 10^{19}$
9	1.2118 $\times 10^{23}$
10	6.8906 $\times 10^{27}$

Appendix E

The Paczyński Presentation

In his early discussion of the effects of gravitational radiation on the evolution of close binaries, Paczyński (1967) demonstrated an appreciation of many of the concepts that have been discussed in the body of this paper, although at the time his analysis was directed primarily to WZ Sge, a cataclysmic variable with an orbital period $P = 81.6$ minutes (gravitational-wave frequency, $f = 4.1 \times 10^{-4}$ Hz). The following brief review of Paczyński's (1967) work illustrates the connection between his derivations and ours, and is presented in an effort to properly credit his early insights into this problem.

In connection with the detached inspiral phase of a binary system's evolution, equation (7) of Paczyński (1967) identifies an evolutionary timescale T_0 that is precisely the same as the quantity, $\tau_{\rm chirp}$, that is defined by our Eq. (3.6). His expression (5) for the time-rate-of-change of the system's orbital angular momentum is also equivalent to our Eq. (3.8), that is,

$$\frac{dJ_{\rm orb}}{dt} = -\frac{J_0}{8\tau_{\rm chirp}} = -\Big[\frac{32}{5}\frac{(2\pi G)^{7/3}}{c^5}\Big] M_{\rm tot}^{10/3} Q^2 P^{-7/3}\,, \tag{E.1}$$

where,

$$P \equiv \frac{2\pi}{\Omega_{\rm orb}} = \frac{2}{f}\,. \tag{E.2}$$

In discussing how the cumulative effect of such a loss of angular momentum might be detectable with ground-based optical telescopes, Paczyński (1967) points out that a shift in orbital phase of an eclipsing binary system (such as WZ Sge) could be observed as an "$(O-C)$" deviation of the observed time of the eclipse. If the observed "$(O-C)$" time that appears in Paczyński's expression (10) is set equal to $P/8 = 1/(4f)$ in order to represent a phase difference of $\pi/2$ radians in the corresponding gravitational-wave signal, then it is easy to show that the quantity labeled ΔT in his expression (10) is precisely the same as the time that we have referred to as $t_{\rm O-C}$ in our Eq. (4.7).

In his discussion of the CMT phase of the evolution of a semi-detached binary system, Paczyński (1967) appreciated that the system would evolve in such a way that the radius of the donor remains in marginal contact with its Roche lobe (*i.e.*, $R_d = R_L$). This assumption also provides the foundation of our discussion in §2.1 and §2.2. However, Paczyński utilized expressions for the white dwarf mass-radius relationship and for the function $R_L(q)$ that are somewhat simpler than the ones we have adopted. Specifically, instead of our Eq. (2.4), Paczyński used (see his expression 13, but note that there is a typographical error in the

numerator of his formula: M_1 should have been $M_2 = M_d$),

$$\frac{R_L}{a} = \frac{2}{3^{4/3}}\Big(\frac{M_d}{M_{\rm tot}}\Big)^{1/3} = \frac{2}{3^{4/3}}\Big(\frac{q}{1+q}\Big)^{1/3}, \tag{E.3}$$

and instead of our Eq. (2.3), he used (see his expression 12),

$$\frac{R_d}{R_\odot} = 1.26\times 10^{-2}(1+X)^{5/3}\Big(\frac{M_d}{M_\odot}\Big)^{-1/3}, \tag{E.4}$$

where X is the star's hydrogen mass-fraction. Paczyński constructed the former expression empirically from Kopal's (1959) tabular data; and an equivalent form of the latter expression can be derived from our more general mass-radius relationship (2.3) by assuming $M_p \ll M_d \ll M_{\rm ch}$. Setting $R_d = R_L$ and using Eqs. (1.6) and (E.2) to express a in terms of P, we obtain Paczyński's expression (14),

$$\frac{M_d}{M_\odot} = \frac{18\pi}{P}\Big(\frac{0.0126}{2}\Big)^{3/2}\Big(\frac{R_\odot^3}{GM_\odot}\Big)^{1/2}(1+X)^{5/2} = \frac{45.3}{P_{\rm sec}}(1+X)^{5/2}\,, \tag{E.5}$$

where $P_{\rm sec}$ is the orbital period expressed in seconds.

From expression (E.4), we immediately deduce that,

$$\zeta_d = \frac{\partial \ln R_d}{\partial \ln M_d} = -\frac{1}{3}\,. \tag{E.6}$$

Rewriting the orbital separation a in terms of $J_{\rm orb}$, Q, and $M_{\rm tot}$ in Eq. (E.3),

$$R_L = \frac{2}{3^{4/3}}\Big[\frac{J_{\rm orb}^2}{GM_{\rm tot}^3}\Big]q^{5/3}(1+q)^{-11/3}\,, \tag{E.7}$$

we also deduce that,

$$\zeta_L = \frac{\partial \ln R_L}{\partial \ln M_d} = (1+q)\frac{\partial \ln R_L}{\partial \ln q} = 2q - \frac{5}{3}\,. \tag{E.8}$$

Hence, for Paczyński's model of a mass-transferring binary system,

$$(\Delta\zeta)_{\rm Pac} = \zeta_d - \zeta_L = \frac{2}{3}(2-3q)\,, \tag{E.9}$$

which in combination with Eq. (3.19) leads to the predicted evolutionary behavior,

$$\Big[\frac{d\ln f}{dt}\Big]_{\rm Pac} \approx -\frac{3}{16\tau_{\rm chirp}}\Big(1-\frac{3}{2}q\Big)^{-1}. \tag{E.10}$$

Realizing that $d\ln P/dt = -d\ln f/dt$, this expression in combination with relations (3.6), (1.6), and (E.2) gives,

$$\begin{aligned}\Big[\frac{dP}{dt}\Big]_{\rm Pac} &\approx \Big[\frac{48(2\pi)^{8/3}(GM_\odot)^{5/3}}{5c^5}\Big]\Big(\frac{M_{\rm tot}}{M_\odot}\Big)^{-1/3}\Big(\frac{M_aM_d}{M_\odot^2}\Big)\Big(1-\frac{3}{2}q\Big)^{-1} \\ &\quad P^{-5/3} \qquad (E.11)\\ &= 1.85\times 10^{-6}\Big(\frac{M_{\rm tot}}{M_\odot}\Big)^{-1/3}\Big(\frac{M_a}{M_\odot}\Big)\Big(\frac{M_d}{M_\odot}\Big)\Big(1-\frac{3}{2}q\Big)^{-1} \\ &\quad P_{\rm sec}^{-5/3}\,. \qquad (E.12)\end{aligned}$$

Then, using expression (E.5) to express $(M_d/M_\odot)$ in terms of P gives,

$$\Big[\frac{dP}{dt}\Big]_{\rm Pac} \approx 8.38\times10^{-5}(1+X)^{5/2}\Big(\frac{M_{\rm tot}}{M_\odot}\Big)^{-1/3}\Big(\frac{M_a}{M_\odot}\Big)\Big(1-\frac{3}{2}q\Big)^{-1} P_{\rm sec}^{-8/3}\,. \tag{E.13}$$

Paczyński's (1967) expression (25) is an application of this general formula to the specific system, WZ Sge, for which he took $P_{\rm sec} = 4.9\times10^3$ and assumed $q \ll 1$, hence also, $M_{\rm tot} \approx M_a$. From expression (E.5), Paczyński realized that $d\ln M_d/dt = -d\ln P/dt$; hence, he was also able to derive an expression for WZ Sge's mass-transfer rate. He realized as well that, for $q \ll 1$, the rate of period (and frequency) change would be a factor of (-2) larger if there were no mass transfer, that is, if WZ Sge was a detached system undergoing inspiral. Here, this is clear from a comparison of our Eq. (3.10) with expression (E.10).

Adopting the above expressions, we can gather together a set of three algebraic relations that can be used to decipher the distance r to a DWD system, as well as the system mass $M_{\rm tot}$ and mass ratio q, given observational measurements of $h_{\rm norm}$, f, and $f^{(1)}$. Combining Eq. (E.10) with Eq. (3.6), we can write

$$rh_{\rm norm} = \frac{5c}{12\pi^2}\Big[\frac{-f^{(1)}}{f^3}\Big]\Big(1-\frac{3}{2}q\Big)\,. \tag{E.14}$$

Because the donor in a DWD system can be safely assumed to have a hydrogen mass-fraction $X = 0$, Eq. (E.5) takes the form,

$$GM_{\rm tot} = \alpha\Big(\frac{1+q}{q}\Big)f\,, \tag{E.15}$$

where, $\alpha \equiv 0.0141(GM_\odot R_\odot^3)^{1/2}$. Finally, from Eq. (2.1) we can write,

$$(GM_{\rm tot})^5 = \frac{1}{64\pi^2}\Big[\frac{(rh_{\rm norm})^3c^{12}}{Q^3f^2}\Big]\,. \tag{E.16}$$

Combining these three expressions gives q in terms of f and $f^{(1)}$ through the nonlinear relation,

$$q^2(1+q)\Big(1-\frac{3}{2}q\Big)^3 = \Big[\frac{2^{12}3^3\pi^8\alpha^5}{5^3c^{15}}\Big]\frac{f^{16}}{[-f^{(1)}]^3}\,. \tag{E.17}$$

Once q has been determined, the calculation of $M_{\rm tot}$ and r is straightforward.

Appendix F

Letter of Permission

American Astronomical Society
2000 Florida Avenue, NW
Suite 400
Washington, DC 20009-1231

tel 202.328.2010
fax 202.234.2560

aas@aas.org
www.aas.org

November 15, 2006

K. Ravi Kumar
Department of Physics and Astronomy
202 Nicholson Hall
Tower Drive
Louisiana State University,
Baton Rouge, LA - 70803-4001

Ravi Kumar Kopparapu,

By notifying the AAS that you plan to use the following *ApJ* paper, you have fulfilled all necessary obligations for release of copyright.

Population Boundaries for Galactic White Dwarf Binaries in LISA's Amplitude-Frequency Domain., Ravi Kumar Kopparapu and Joel E. Tohline, MS# 65935,
Estimated 9 Printed Pages + 3 Color Figure(s) + 0 Machine
Readable Table(s) + 0 (Online Figures)

All reproduced material must be properly identified by the citation of the original publication and may carry the indication, "reproduced by permission of the AAS."

Should you need any further information, please do not hesitate to contact me.

Sincerely,

Crystal Tinch
Publications Specialist

Vita

Ravi Kumar Kopparapu was born in Vijayawada, India, on June 11, 1976. He earned his bachelor's degree in electronics in 1996 from Sarada College, affiliated to Nagarjuna University. From 1996-1998, Ravi did his master's in physics with specialization in astrophysics from University of Pune, India. Two years later, in the Fall of 2000, Ravi joined the graduate school at Louisiana State University. He expects to receive his doctorate degree in Decemeber 2006.